AIAA JOURNAL
Vol. 49, No. 4, April 2011

Comparison of Node-Centered and Cell-Centered Unstructured Finite Volume Discretizations: Inviscid Fluxes

Boris Diskin*
National Institute of Aerospace, Hampton, Virginia 23681
and
James L. Thomas†
NASA Langley Research Center, Hampton, Virginia 23681

DOI: 10.2514/1.J050897

Nominally second-order cell-centered and node-centered approaches are compared for unstructured finite volume discretization of inviscid fluxes in two dimensions. Three classes of grids are considered: isotropic grids in a rectangular geometry, anisotropic grids typical of adapted grids, and anisotropic grids over a curved surface typical of advancing-layer grids. The classes contain regular and irregular grids, including mixed-element grids and grids with random perturbations of nodes. Complexity, accuracy, and convergence of defect-correction iterations are studied. Deficiencies of specific schemes, such as instability, accuracy degradation, and/or poor convergence of defect-correction iterations, have been observed in computations and confirmed in analysis. All schemes may produce large relative gradient-reconstruction errors on grids with perturbed nodes. On advancing-layer grids, a local approximate-mapping technique based on the distance function restores gradient-reconstruction accuracy and fast convergence of defect-correction iterations. Among the considered scheme, the best cell-centered and node-centered schemes, which are low-complexity, stable, robust, and uniformly second-order-accurate, are recommended.

Nomenclature

$A, B, C, D, E, F, G, H, I, J, K, L$	=	primal cell centers
$\mathcal{A}$	=	aspect ratio
a, b	=	reconstructed gradient components
$\mathbf{a}$	=	velocity vector
E_d	=	discretization error
E_{rel}	=	relative gradient error
f	=	forcing function
h	=	local mesh size
h_r, h_θ	=	radial and circumferential mesh spacing, respectively
h_x, h_y	=	Cartesian mesh sizes in x and y directions, respectively
$\hat{h}_y$	=	minimal mesh spacing on stretched grids
L	=	characteristic scale of domain
L_d^h	=	linearized driver scheme
N	=	total number of mesh points
$\mathbf{n}$	=	outward directed-area vector
$\hat{\mathbf{n}}, \hat{\mathbf{t}}$	=	unit vectors normal and tangential to the boundary, respectively
$\bar{\mathbf{n}}$	=	outward unit normal vector
N_x, N_y	=	number of grid points in x and y directions, respectively
R	=	radius of curvature
r, θ	=	polar coordinates
$\mathbf{r}$	=	coordinate vector
$\mathbf{r}^*$	=	point on boundary closest to field point $\mathbf{r}$
$R^h(\cdot)$	=	discrete residual
s	=	distance to designated boundary
$\bar{s}$	=	small horizontal node perturbation
s_f	=	distance from face center to closest boundary
U	=	exact solution
U_L, U_R	=	left and right solution reconstructions
U^h	=	discrete solution
U^r	=	linear solution reconstruction
u^h	=	approximate discrete solution
V	=	measure of control volume
v^h	=	correction to approximate discrete solution
x, y	=	Cartesian coordinates
β	=	stretching factor
Γ	=	curvature-induced grid deformation parameter
μ_k	=	weights in least-squares minimization
ξ, η	=	local coordinates
ρ	=	random number $\in [-1, 1]$
$\Omega, \partial\Omega$	=	control volume and control-volume boundary, respectively
0, 1, 2, 3, 4, 5, 6, 7, 8, 9, 10, 11, 12	=	grid nodes
∇	=	gradient operator
∇_r	=	reconstructed gradient
$\lvert\cdot\rvert$	=	vector length
$\lVert\cdot\rVert$	=	norm of interest, e.g., L_1 or L_∞

Subscripts

numerals	=	stencil points
f	=	face center

Presented as Paper 2010-1079 at the 48th Aerospace Science Meeting and Exhibitions, Orlando, FL, 4–7 January 2010; received 31 August 2010; accepted for publication 25 November 2010.

*100 Exploration Way; University of Virginia, Department of Mechanical and Aerospace Engineering, Charlottesville, Virginia 22904; bdiskin@nianet.org. Senior Member AIAA.

†Computational AeroSciences Branch, Mail Stop 128; james.l.thomas@nasa.gov. Fellow AIAA.

I. Introduction

BOTH node-centered (NC) and cell-centered (CC) finite volume discretization (FVD) schemes are widely used for complex three-dimensional (3-D) turbulent-flow simulations in aerospace applications. The relative advantages of the two approaches have been extensively studied [1–3] in the search for methods that are

Table 1 Acronyms used for identification of discretization schemes

Acronym	Description
AM	*Approximate mapping* can be applied on grids of class (C) with any scheme. In this paper, AM is used in NC-ULSQ-AM, CC-NN-AM, CC-FAULSQ-AM, and CC-SA-AM schemes.
CC	*Cell-centered* discretization uses primal grid cells as control volumes.
CLIP	*Clipping* can be used in conjunction with CC-NA schemes.
EG	*Exact gradient* can be applied for CC discretizations and used in reconstruction for reference.
FA	*Full-augmentation* stencil can be applied only for CC discretizations. FA indicates that the stencil for least-squares gradient reconstruction at a cell is large and involves all cells sharing a node with the considered cell.
NA	*Node averaging* can be applied only for CC discretizations. Solutions are first reconstructed at nodes using an averaging procedure.
NC	*Node-centered* discretization uses median-dual cells as control volumes.
NN	*Nearest-neighbor* stencil can be applied only for CC discretizations. NN indicates that the stencil for least-squares gradient reconstruction at a cell is small and involves only neighboring cells sharing a face with the considered cell.
SA	*Smart-augmentation* stencil can be applied only for CC discretizations. SA indicates that the stencil for least-squares gradient reconstruction is a small subset of the FA stencil and moderately larger than the NN stencil.
ULSQ	*Unweighted least-squares* gradient reconstruction employs a least-squares minimization problem with a cost functional that uses unweighted (equal) contributions from all stencil points. In this paper, the following schemes use the ULSQ method: NCULSQ, CC-FA-ULSQ, CC-SA, and CC-NN.
WLSQ	*Weighted least-squares* gradient reconstruction employs a least-squares minimization problem with a cost functional that uses weighted contributions from stencil points. The weights are inversely proportional to the squared distances to the stencil center. In this paper, the NC-WLSQ and CC-FA-WLSQ schemes use the WLSQ method.

accurate, efficient, and robust over the broadest possible range of grid and solution parameters, but a consensus has not emerged. One of the difficulties in assessing the two approaches is that comparative calculations were not completed in a controlled environment; that is, computations were made with different codes and different degrees of freedom, and the exact solutions were not known.

In this paper, a subset of the discretization elements needed in turbulent-flow simulations, namely, that of the inviscid discretization, is studied in a controlled environment. This paper is the second in a series of papers comparing CC and NC finite volume schemes. It follows a previous study [3] that considered viscous discretizations. The ultimate objective of the effort is to identify methods suitable for a uniformly second-order-accurate and efficient unstructured-grid solver for the Reynolds-averaged Navier–Stokes equations.

In this work, a linear convection equation,

$$(\mathbf{a} \cdot \nabla U = f) \tag{1}$$

serves as a model for inviscid fluxes. Here, $\mathbf{a}$ is a constant velocity vector and f is a forcing function. The method of manufactured solution is used, so the exact solutions are known and chosen to be smooth on all grids considered; that is, no accuracy degradation occurs because of a lack of solution smoothness. Computational studies are conducted on two-dimensional (2-D) grids ranging from structured (regular) grids to irregular grids composed of arbitrary mixtures of triangles and quadrilaterals. Highly irregular grids are deliberately constructed through random perturbations of structured grids to bring out the worst possible behavior of the solution. Three classes of grids are considered. Class (A) involves isotropic grids in a rectangular geometry. Class (B) involves highly anisotropic grids, typical of those encountered in grid adaptation. Class (C) involves advancing-layer grids varying strongly anisotropically over a curved body, typical of those encountered in high-Reynolds-number turbulent-flow simulations.

Eight nominally second-order schemes are considered: two representative NC schemes with weighted least-squares (WLSQ) and unweighted least-squares (ULSQ) methods for gradient reconstruction and six CC schemes. The CC schemes include node-averaging (NA) schemes, with and without clipping, and four least-squares gradient reconstruction schemes that are named according to the stencil used for the least-squares fit: a nearest-neighbor (NN) scheme using only face-neighboring cells, a smart-augmentation (SA) scheme moderately augmenting the NN stencil, and two full augmentation (FA) schemes, with and without weighting, using larger stencils (including all node-sharing cells). For the grids of class (C), the approximate-mapping (AM) technique [3] is used to improve gradient reconstruction accuracy and convergence of defect-correction iterations (DCIs). The technique is based on the distance function (the distance from a field point to the nearest surface) commonly available in practical codes and can be

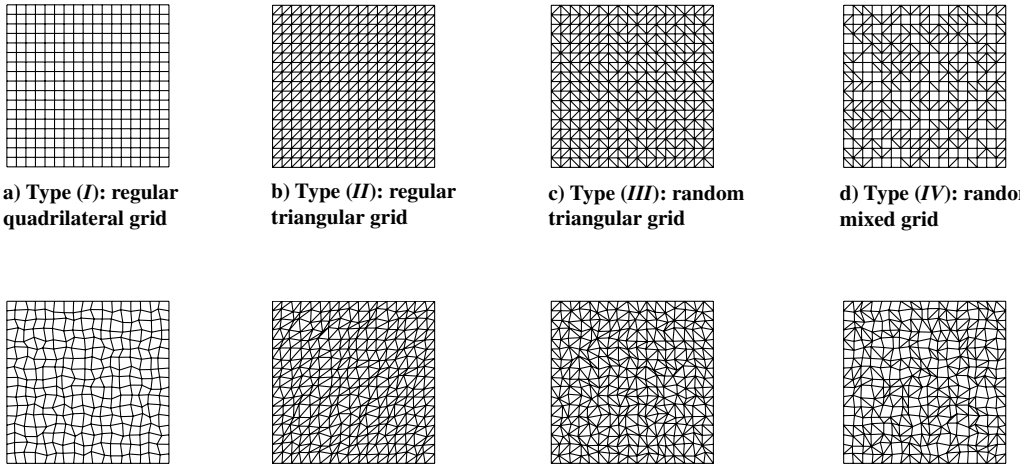

a) Type (*I*): regular quadrilateral grid

b) Type (*II*): regular triangular grid

c) Type (*III*): random triangular grid

d) Type (*IV*): random mixed grid

e) Type (I_p): perturbed quadrilateral grid

f) Type (II_p): perturbed triangular grid

g) Type (III_p): perturbed random triangular grid

h) Type (IV_p): perturbed random mixed grid

Fig. 1 Typical regular and irregular grids.

used with any scheme. Individual schemes are identified by a combination of acronyms shown in Table 1.

The properties to be compared in this study are computational complexity (operation count), discretization accuracy, and convergence rates of the defect-correction method with a first-order driver. The material in this paper is presented in the following order. Section II introduces the computational grids used in the current study. A brief explanation of finite volume discretizations in Sec. III is followed by the estimates of discretization complexity for 2-D and 3-D grids in Sec. IV. Section V outlines the analysis methods used in this study. Section VI contains results on the accuracy of finite volume solutions and gradients, and on convergence rates of the defect-correction method observed on grids of class (A). Section VII compares the finite volume discretizations on grids of class (B). Section VIII provides comparisons on grids of class (C). Conclusions and recommendations are offered in Sec. IX. Detrimental effects of clipping on the accuracy of the CC-NA scheme are shown in Appendix A. Appendix B analyzes the instability of finite volume schemes with WLSQ gradient reconstruction on high-aspect-ratio grids with small perturbations.

II. Grids

This paper studies FVD schemes for inviscid fluxes on regular and irregular grids classified in [3]. Four basic grid types are considered: (I) regular quadrilateral (i.e., mapped Cartesian) grids; (II) regular triangular grids derived from the regular quadrilateral grids by the same diagonal splitting of each quadrilateral; (III) random triangular grids, in which regular quadrilaterals are split by randomly chosen diagonals, each diagonal orientation occurring with a probability of half; and (IV) random mixed-element grids, in which regular quadrilaterals are randomly split or not split by diagonals (the splitting probability is half; in the case of splitting, each diagonal orientation is chosen with the probability of half). Nodes of any basic-type grid can be perturbed from their initial positions by random shifts, thus leading to four additional perturbed grid types that are designated by the subscript p as (I_p)–(IV_p). The random node perturbation in each dimension is typically defined as $\frac{1}{4}\rho h$, where $\rho \in [-1, 1]$ is a random number and h is the local mesh size along the given dimension. The representative grids are shown in Fig. 1.

Our main interest is the accuracy and efficiency of FVD schemes on general irregular grids with a minimum set of constraints. In particular, grid smoothness is not required, neither on individual grids nor in the limit of grid refinement. The only major requirement for a sequence of refined grids is to satisfy the consistent refinement property [4]. The effective mesh size is computed on each grid as the L_1 norm of the square root of the control volumes.

The discrete solutions are available at locations called data points. For consistency with the 3-D terminology, the 2-D control-volume boundaries are called faces, and the term edge refers to a line, possibly virtual, connecting the neighboring data points. Each face is characterized by the directed-area vector, which is directed outwardly normal to the face with the magnitude equal to the face area.

III. Finite Volume Discretization Schemes

The FVD schemes are derived from the integral form of a conservation law:

$$\oint_{\partial\Omega} U\left(\mathbf{a}\cdot\bar{\mathbf{n}}\,\mathrm{d}s = \int_{\Omega} f\,\mathrm{d}\Omega\right) \tag{2}$$

where Ω is a control volume with boundary $\partial\Omega$, $\bar{\mathbf{n}}$ is the outward unit normal vector, and $\mathrm{d}s$ is the area differential. The general FVD approach requires partitioning the domain into a set of nonoverlapping control volumes and numerically implementing Eq. (2) over each control volume. The control volumes used for NC formulations are referred to as dual cells to distinguish them from primal cells used as control volumes in CC formulations.

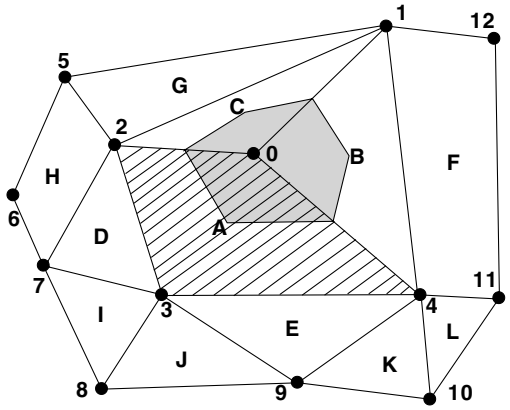

Fig. 2 Control volume partitioning for finite-volume schemes.

CC discretizations assume solutions are defined at the centers of the primal cells. The cell center coordinates are typically defined as the averages of the coordinates of the cell's vertexes. Note that, for quadrilateral cells, cell centers are not necessarily centroids. NC discretizations assume solutions are defined at the primal mesh nodes. For NC schemes, control volumes are constructed around the mesh nodes by the median-dual partition: the centers of primal cells are connected with the midpoints of the surrounding faces. These nonoverlapping control volumes cover the entire computational domain and compose a mesh that is dual to the primal mesh. Both CC and NC control-volume partitions are illustrated in Fig. 2; 0–12 and *A*-*L* denote grid nodes and primal cell centers, respectively. The control volume (dual cell) for a NC discretization around grid node 0 is shaded. The control volume (primal cell) for a CC discretization around cell center *A* is hashed.

The flux, $U^h(\mathbf{a}\cdot\bar{\mathbf{n}})$, at a control-volume face is computed according to the flux-difference-splitting scheme [5]:

$$U^h\big(\mathbf{a}\cdot\bar{\mathbf{n}} = \tfrac{1}{2}\big(U_L + U_R\big(\mathbf{a}\cdot\bar{\mathbf{n}} - \tfrac{1}{2}|(\mathbf{a}\cdot\bar{\mathbf{n}}|(U_R - U_L))\big)\big)\big) \tag{3}$$

where first and second terms represent the flux average and the dissipation, respectively; U_L and U_R are the left and right solutions linearly reconstructed at the face by using solutions defined at the control-volume centers and solution gradients reconstructed at each control volume. Various FVD schemes differ in the way they reconstruct gradients at the control volumes.

For CC schemes, the face-based flux integration over a control-volume face is approximated as the flux computed at the face center multiplied by the face area. The integration scheme is second-order accurate on grids of all types.

For NC schemes, the edge-based flux integration scheme approximates the integrated flux through the two faces linked at an edge midpoint by $U^h(\mathbf{a}\cdot\mathbf{n})$, computed at the edge midpoint where $\mathbf{n}$ is the combined-directed-area vector. The integration scheme is computationally efficient and second-order accurate on regular quadrilateral and simplicial grids: types (I), (II), (III), (II_p), and (III_p). The integration accuracy degenerates to first order on mixed-element and perturbed quadrilateral grids of types (IV), (IV_p), and (I_p) [4,6,7]. Note that NC face-based integration schemes that avoid accuracy degradation can be constructed but at a higher cost [7] (see also estimates in Sec. IV).

The forcing term integration over the cell is approximated as the value at the cell center multiplied by the cell volume:

$$V = \int_{\Omega} \mathrm{d}\Omega \tag{4}$$

This approximation is locally second-order accurate when the cell center coincides with the centroid. On general irregular grids, the cell center is not necessarily the centroid, and the approximation becomes locally first-order accurate. However, with grid irregularities introduced locally and randomly (thus, implying a zero-mean distribution of the deviations between cell centers and centroids), the integral of

the forcing term over any subdomain of size $O(1)$ is approximated with second order.

The specific schemes presented in the following sections are either representative of the schemes used in the state-of-the-art industrial codes or new developments promising significant improvements in solution accuracy, efficiency, and/or robustness.

A. Cell-Centered Schemes

1. *Node-Averaging Schemes*

In CC-NA schemes, solution values are first reconstructed at the nodes from the surrounding cell centers. With respect to Fig. 2, the solution at node 0 is reconstructed by averaging solutions defined at the cell centers A, B, and C. The commonly used solution reconstruction [8–10] is an averaging procedure that is based on a constrained optimization to satisfy some Laplacian properties. The scheme is second-order accurate and stable when the coefficients of the introduced pseudo-Laplacian operator are close to unity. It has been shown [11] that this averaging procedure is equivalent to an ULSQ linear fit.

The gradient of the solution U at the cell Ω is reconstructed by the Green–Gauss formula:

$$\nabla U = \frac{1}{V}\oint_{\partial\Omega} U\bar{\mathbf{n}}\,\mathrm{d}s \tag{5}$$

For second-order accuracy, the solution at a face is computed by averaging the values at the face nodes, and the integral over the face is approximated by the product of the solution and the face directed area. For simplicial grids, an explicit formula relating the gradient to the nodal solution values is given elsewhere [10].

On highly stretched and deformed grids, some coefficients of the pseudo-Laplacian may become negative or larger than two, which has a detrimental effect on stability and robustness [12,13]. Holmes and Connell [8] proposed to enforce stability by clipping the coefficients between zero and two. The CC-NA scheme with clipping (CC-NA-CLIP) represents a current standard in practical computational fluid dynamics codes involving CC finite volume formulations [14]. As shown further in the paper, clipping seriously degrades the accuracy of the solution.

2. *Least-Squares Schemes*

An alternative approach relies on a least-squares method for gradient reconstruction, in which the linear approximation obtained at a control volume coincides with the solution value at the control-volume center. In this paper, both WLSQ and ULSQ methods are considered. In the WLSQ method, the contributions to the minimized functional are weighted, with weights inversely proportional to the distance from the control-volume center. In the unweighted method, all contributions are equally weighted.

The complexity, accuracy, and robustness of the solvers using a least-squares method for gradient reconstruction may vary, depending on the choice of the stencils for the least-squares minimization. Below, three types of stencils are considered. The NN stencil includes only centers of face-neighbor cells. The FA stencil includes all the cells that share a vertex with the given cell: i.e., all the cells involved in CC-NA gradient reconstruction. The SA stencil employs only a small portion of the cells used in the corresponding FA stencil. The data point of the central cell is also referred to as the stencil center.

Defect-correction iterations with a first-order driver are widely used for solution of FVD schemes. It has been observed that defect-correction iterations may become slow or even diverge for the CC-NN scheme, but the defect-correction iteration rates are always fast for the CC-FA-ULSQ scheme. This observation motivated the development of the CC-SA scheme with low complexity and fast defect-correction iteration rates.

The version of the CC-SA scheme used in this paper has been chosen for simplicity of implementation. It uses a predefined small-size augmentation and applies augmentation to all gradient stencils. Initially, the SA stencil associated with a cell is identical to the NN stencil. The initial stencil is augmented with a few cells, one added cell per vertex. For each cell vertex, the cell added to the SA gradient stencil is the most distant from the stencil center of all the cells surrounding the vertex. The CC-SA stencil size approximately doubles the stencil size of the CC-NN scheme, but it is much smaller than the CC-FA stencil size. Addition of the most distant cells is guided by the observation that the distant points carry most of the weight in the ULSQ gradient reconstruction when the obtained linear approximation coincides with the solution value at the stencil center. For cell center A in Fig. 2, the NN stencil includes neighbors B, C, D, and E; the SA stencil adds neighbors H, I, and L; and the FA stencil includes (additionally) neighbors F, G, J, and K.

The complexity of the CC-SA scheme can be further reduced with an appropriate test performed in local computational windows. In [15], a simple test based on a single-cell computational window was applied to optimize the stencil size. This single-cell approach was efficient for many computations, but it has been recently found to not be sufficiently robust. Alternative tests with larger computational windows have been found to be sufficiently robust, but they are not pursued in this paper.

B. Node-Centered Schemes

For the NC computations, the current standard employs a least-squares gradient reconstruction. The typical stencil at a control volume involves all nodes linked by an edge. For example, with reference to Fig. 2, the least-squares fit for the shaded control volume centered at node 0 includes nodes 1, 2, and 4. Both WLSQ and ULSQ methods are evaluated.

C. Approximate-Mapping Method

A general approximate-mapping method has been introduced in [3]. The method constructs a local mapping based on a distance function that supplies the distance from a field node to designated boundaries that is readily available in practical codes. The approximate-mapping method applies the least-squares minimization in a local coordinate system (ξ, η), where η is the coordinate normal to the boundary and ξ is the coordinate parallel to the boundary (see sketch in Fig. 3). At each control volume, the unit vector normal to the boundary $\hat{\mathbf{n}}_0$ is constructed as

$$\hat{\mathbf{n}}_0 = \left(\mathbf{r}_0 - \mathbf{r}_0^*/|\mathbf{r}_0 - \mathbf{r}_0^*|\right) \tag{6}$$

where the position of the control-volume center is denoted as $\mathbf{r}_0$ and the position of the closest point on the boundary is denoted as $\mathbf{r}_0^*$. The unit vector normal to $\hat{\mathbf{n}}_0$ is denoted as $\hat{\mathbf{t}}_0$. To construct the least-squares minimization at the control volume, the local coordinates of a stencil point $\mathbf{r}_i$ are defined as

$$\xi_i = \left(\mathbf{r}_i - \mathbf{r}_0 \cdot \hat{\mathbf{t}}_0\right) \tag{7}$$

$$\eta_i = (s_i - s_0) \tag{8}$$

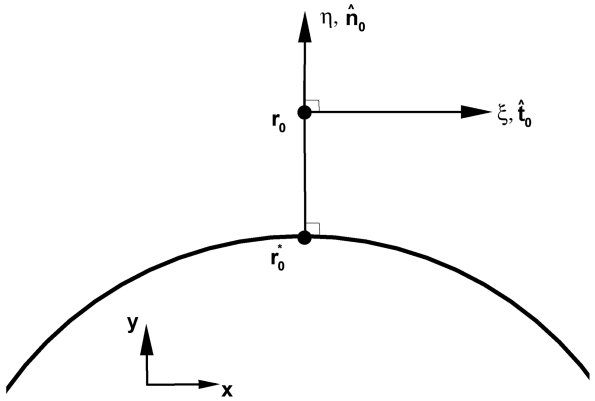

Fig. 3 Sketch of coordinate system used in the approximate-mapping method.

where s_i approximates the distance function at location $\mathbf{r}_i$. In the current version, the distance function is always defined at mesh nodes. For CC schemes, the distance function at the cell center is calculated by averaging the distance functions defined at cell vertexes. Thus, the η coordinate corresponds to the distance from the boundary, and the ξ coordinate is the projection onto the plane parallel to the surface at $\mathbf{r}_0$. The least-squares minimization yields gradients in the (ξ, η) directions or, equivalently, through a coordinate rotation in the (x, y) Cartesian directions.

To reconstruct an interior state for the flux computation at a control-volume face location $\mathbf{r}_f$ the coordinates associated with the mapping at $\mathbf{r}_0$ are introduced as

$$\xi_f^0 = \left(\mathbf{r}_f - \mathbf{r}_0 \cdot \hat{\mathbf{t}}_0\right) \tag{9}$$

$$\eta_f^0 = \left(s_f - s_0\right) \tag{10}$$

The coordinate s_f is approximated as

$$s_f = (s_0 + s_1/2) \tag{11}$$

where, for NC schemes, s_0 and s_1 correspond to the distance function of the two nodes defining the edge; for CC schemes, s_0 and s_1 correspond to the nodes defining the face. The interior state is linearly reconstructed using the state at $\mathbf{r}_0$ and gradients in the (ξ, η) directions.

IV. Complexity

In this section, the complexity of FVD schemes is evaluated per degree of freedom. On a given grid, CC schemes typically have many more degrees of freedom than NC schemes.

A. Flux Integration Complexity

In this section, the complexity associated with flux integration in 3-D is estimated. The complexity is measured as the number of flux-reconstruction instances required for one residual evaluation. Flux reconstructions are the main contributors to the operation counts associated with flux integration. Three types of primal meshes are considered: 1) fully tetrahedral, 2) fully prismatic, and 3) fully hexahedral.

An underlying Cartesian grid is considered and split into the various elements. The splitting into tetrahedra assumes each hexahedral cell defined by the grid is split into five tetrahedra, with one of the tetrahedra being completely interior to the hexahedral cell (i.e., its faces are not aligned with any of the hexahedral-cell faces; see Fig. 4). Other partition strategies are possible but not considered.

Table 2 shows complexity estimates for one CC and two NC FVD schemes. Only interior discretizations are estimated as boundary effects are neglected. The CC formulation uses a face-based flux integration scheme with one flux reconstruction per control face. The NC schemes assume a median-dual partition of the domain and use both an edge-based and a face-based flux integration.

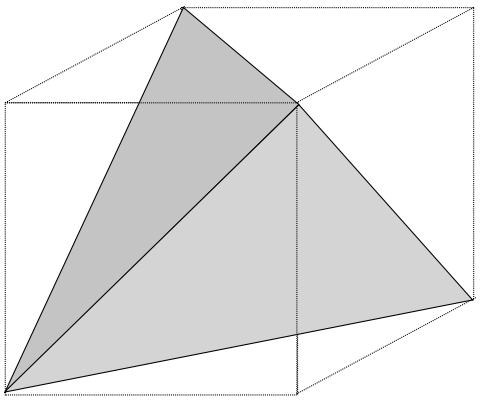

Fig. 4 Splitting of a hexahedral cell into five tetrahedra.

Table 2 Number of flux-reconstruction instances per equation for FVD schemes with precise (watertight) definition of the control-volume boundary; in parentheses: the number of flux-reconstruction instances with planar approximations to the control-volume boundary

Elements	CC face-based flux integration	NC edge-based flux integration	NC face-based flux integration
Tetrahedral	4 (4)	12	120 (60)
Prismatic	8 (5)	8	72 (36)
Hexahedral	12 (6)	6	48 (24)

In a median-dual partition, the constituent dual control volumes are bounded by generally nonplanar dual faces formed by connecting three types of points: 1) edge midpoints, 2) element-face centroids, and 3) element centroids. The edge-based flux integration approximates integration over all of the constituent dual faces adjacent to an edge by a product of the flux evaluated at the edge midpoint and a lumped directed area. The face-based flux integration multiplies fluxes reconstructed at each of the constituent dual faces with the corresponding local directed areas. For the present estimation, each flux-reconstruction instance requires the same operation count.

Two estimates of complexity are given. The first estimate assumes that any constituent quadrilateral face in the control surface is broken into two triangular faces. The second estimate (in parentheses) assumes any constituent quadrilateral face is approximated as planar. The former is required to ensure a precise (watertight) definition of the control surface and can serve as a measure of the complexity in integration of the physical flux terms. The latter can serve as an estimate of the complexity associated with numerical dissipation terms, in which details of the control surface can be neglected.

The complexities of CC and NC edge-based-flux-integration schemes are reasonably close. Unfortunately, as shown in this paper and previously [4,6,7], the accuracy of NC edge-based-flux-integration schemes degenerates to first order on perturbed quadrilateral and general mixed-element grids. To maintain second-order accuracy on general grids, one can employ the NC scheme with a face-based flux integration, but the integration complexity of this formulation substantially exceeds the complexity of the CC scheme. These results are in agreement with the observations made by Delanaye and Liu [1], leading to their selection of a CC discretization.

B. Size of Inviscid Stencil

Another important measure of complexity of an FVD scheme is the size of the full-linearization stencil. The size of the 2-D and 3-D full-linearization stencils is examined for inviscid CC and NC FVD schemes. Cartesian meshes are split into triangular and tetrahedral elements, as in the previous section, again neglecting boundary effects. Estimates of the stencil complexity are compared with

Table 3 Average size of the inviscid first-order FVD stencil on triangular/tetrahedral grids in 2-D/3-D

Elements	NC	CC
Estimate 2-D	7	4
Estimate 3-D	13	5
Numerical 3-D	14	5

Table 4 Average size of the inviscid second-order stencil for 2-D/3-D discretizations with triangular/tetrahedral elements

Elements	NC	CC-NA	CC-NN	CC-SA
Estimate 2-D	23	25	9	18
Estimate 3-D	75	139	15	28
Numerical 3-D	63	118	15	27

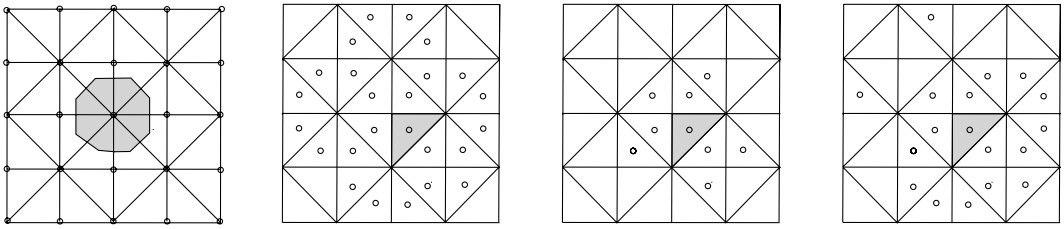

a) NC scheme b) CC-FA and CC-NA schemes c) CC-NN scheme d) CC-SA scheme

Fig. 5 Inviscid 2-D stencil for the shaded control volume.

numerical calculations on an actual 3-D grid that includes boundary effects. The grid is a fully tetrahedral grid composed of 16,391 nodes.

For the inviscid discretization, the DCI with a first-order driver is generally used to converge the residual. Thus, it is important to consider first-order and second-order linearizations. For the first-order CC FVD scheme, the size of the linearization stencil is simply the number of faces plus one (to account for the central node). For the first-order NC discretization, the size of the linearization stencil is the number of edges connecting to a node plus one. Table 3 shows 2-D and 3-D linearization stencil sizes. The CC discretization has nearly a factor of three smaller stencil in 3-D.

For second-order accuracy, all schemes reconstruct gradients in the control volumes. The NC discretizations use a least-squares approach and require solutions at the neighbor and neighbor-of-neighbor nodes and a correspondingly large linearization stencil. The CC-NA discretizations have even larger linearization stencils that include all cells contributing to solution reconstruction at any node of a face-neighboring cell. Stencils of CC-FA discretizations are the same as CC-NA stencils. The CC-NN discretization requires a much smaller stencil that includes only face-neighbor and neighbor-of-neighbor cells. The CC-SA least-squares stencil includes, additionally, one cell per vertex and approximately doubles the size of the CC-NN stencil. Table 4 shows stencil sizes for 2-D and 3-D. The splittings used in the estimates are shown in Figs. 4 and 5 for 3-D and 2-D, respectively. In 3-D, the CC-SA discretization stencil is more than two times smaller than the NC discretization stencil; the latter, in turn, is significantly smaller than the CC-NA and CC-FA discretization stencils. In both 2-D and 3-D, the CC-NN discretization stencil is the smallest.

For illustration, the 2-D stencils for a single shaded control volume are shown in Fig. 5 for each approach. The stencil sizes are 25, 25, 9, and 18 for the NC, CC-NA, CC-NN, and CC-SA schemes, respectively. Note that the stencil size for the NC control volume with four edges adjacent to the shaded one shown in Fig. 5 is 21; thus, the average of 23 is shown in Table 4.

For 3-D NC schemes, the nodes with 6 and 18 edges have stencil sizes of 57 and 93, respectively. Thus, the average of 75 is shown in Table 4. For the CC-NA and CC-FA schemes, the cells at the corners of the original Cartesian cell have a stencil size of 149, and those fully interior to the original Cartesian cell have a stencil size of 99. Since there is one interior tetrahedron for each of the four corner tetrahedrons, the average of 139 is shown in Table 4. The CC-SA stencil on an interior tetrahedron adds 12 to 15 cells of the CC-NN stencil, resulting in the 27-cell CC-SA stencil. For a corner tetrahedron, the CC-SA stencil includes 13 additional cells and has 28 cells in total. Thus, the rounded average of 28 is shown for the CC-SA scheme in the table. The stencil complexity observed on realistic computational grids is shown in the last row of Table 4 and is reasonably close to the corresponding estimates.

V. Analysis

The accuracy of FVD schemes is analyzed for known exact or manufactured solutions. The forcing function and boundary values are found by substituting this solution into the governing equations, including boundary conditions. The discrete forcing function is defined at the data points. Boundary conditions are overspecified; that is, discrete solutions at boundary control volumes and at their neighbors are specified from the manufactured solution.

A. Discretization Error

The main accuracy measure is the discretization error E_d, which is defined as the difference between the exact discrete solution U^h of the discretized Eq. (2) and the exact continuous solution U to the corresponding differential equations:

$$E_d = U - U^h \tag{12}$$

where U is sampled at data points.

Discretization errors measured on specific grids may depend on particular irregularity patterns. To account for this dependence, all numerical tests are performed stochastically; that is, several grids (ten) with different irregularity patterns are independently generated on each scale (same number of nodes). In all tests, where the variation of a discretization error norm for the same scale is significant, the mean error as well as the maximum and the minimum errors are shown.

B. Accuracy of Gradient Reconstruction

The accuracy of the gradient approximation at a control volume is also important. For second-order convergence of discretization errors, the gradient accuracy is usually required to be at least first order. For each control volume, the accuracy of the gradient is evaluated by comparing the reconstructed gradient $\nabla_r U$ with the exact gradient ∇U computed at the control-volume center. The gradient reconstruction uses a discrete representation (usually injection) of the exact solution U at the data points on a given grid. The accuracy of the gradient reconstruction is measured as the relative gradient error:

$$E_{\text{rel}} = \frac{\|\epsilon_g\|}{\|g\|} \tag{13}$$

where functions ϵ_g and g are the amplitudes of the gradient error and the exact gradient, respectively, evaluated at control-volume centers:

$$\epsilon_g = |\nabla_r U - \nabla U|, \quad \text{and} \quad g = |\nabla U| \tag{14}$$

$\|\cdot\|$ is a norm of interest. In this paper, the gradient errors are measured only at fully interior control volumes.

C. Convergence of Defect-Correction Iterations

Besides accuracy, an important quality of a practical discretization is the availability of an affordable solver. For FVD schemes with low complexity, such as CC-NN and CC-SA, an efficient solution method would directly iterate the target FVD scheme. For FVD schemes with high complexity, such as CC-NA, CC-FA, and NC schemes, direct iterations are not affordable. DCI schemes with linearized first-order drivers are common methods used in practical computations.

Let u^h be the current solution approximation. The DCI method is defined in the following two steps:

1) The correction v^h is calculated from

$$L_d^h v^h = R^h\left(u^h\right) \tag{15}$$

where $R^h\left(u^h\right)$ is the residual of the target FVD scheme and L_d^h is a driver scheme. Equation (15) is solved to zero residual.

2) The current approximation is corrected:

$$u^h = u^h + v^h \tag{16}$$

The DCI method considered in this paper is applied to second-order FVD schemes and uses the corresponding first-order upwind FVD scheme as a driver. In DCI tests, the forcing term and the boundary conditions are set to zero, so the exact solution is zero. The initial solution perturbation is random.

The DCI asymptotic convergence rate is estimated as either the spectral radius of the DCI matrix on a given (small) grid or as the ratio of residuals obtained in the two last iterations performed. Note that convergence observed in individual iterations may significantly differ from the corresponding asymptotic convergence rate. On one hand, the initial convergence is typically fast and, in some cases, the residual tolerance (e.g., machine zero) can be achieved before convergence slows down to the asymptotic rate. On the other hand, some norms of the iteration matrix (e.g., maximum sum of row-entry absolute values) are much larger than the spectral radius, allowing slower convergence rates, or even divergence in individual iterations.

VI. Class (A): Isotropic Grids in Rectangular Geometry

A. Grid Specification

Grids of types (III_p) and (IV_p) are chosen to represent isotropic grids of poor quality. Sequences of consistently refined grids are generated on the unit square $[0, 1] \times [0, 1]$. Irregularities are introduced at each grid independently, so the grid metrics, such as cell volumes and face areas, remain discontinuous on all the grids. The ratio of the neighboring cell volumes can be arbitrarily high. The CC-NA-CLIP scheme clips about 10 and 3% of the interior nodes on grids of types (III_p) and (IV_p), respectively.

B. Gradient Reconstruction Accuracy

On unperturbed isotropic grids of types (I)–(IV) and on perturbed quadrilateral grids of type (I_p), all gradient reconstruction methods provide at least first-order-accurate gradients. Figure 6 shows the convergence of the L_∞ norms of relative gradient errors for the manufactured solution $U = -\cos(2\pi x - \pi y)$ on grids of types (III_p) and (IV_p). Only errors computed with the CC-NA-CLIP scheme do not converge in grid refinement. Similar absence of convergence has been observed and reported previously [3] for gradients reconstructed with the CC-NA-CLIP scheme within control-volume faces. All other methods provide first-order gradient approximations on all isotropic grids.

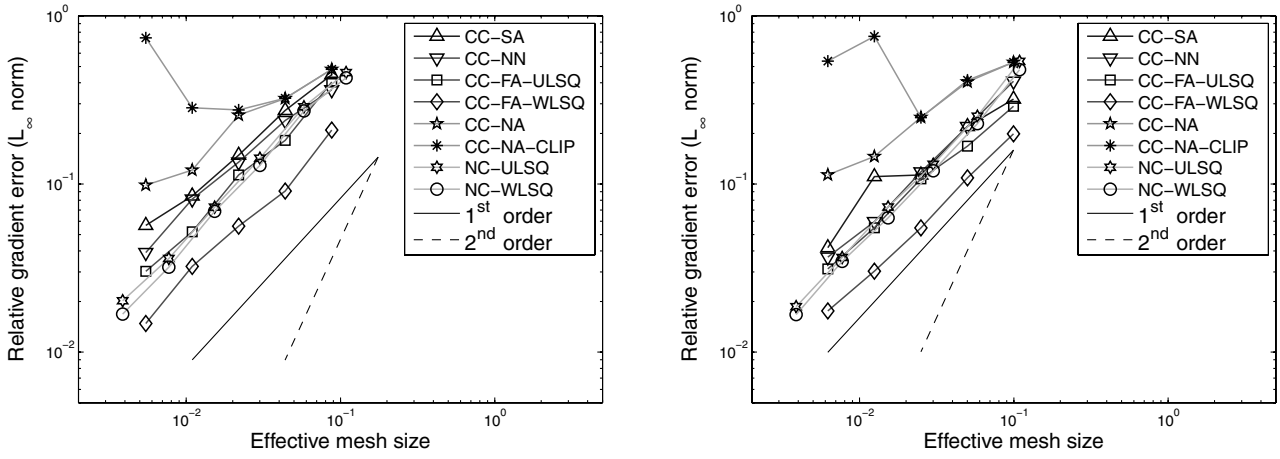

a) Grids of type (III_p) **b) Grids of type (IV_p)**

Fig. 6 Accuracy of gradient reconstruction on isotropic irregular grids. Manufactured solution is $U = -\cos(2\pi x - \pi y)$.

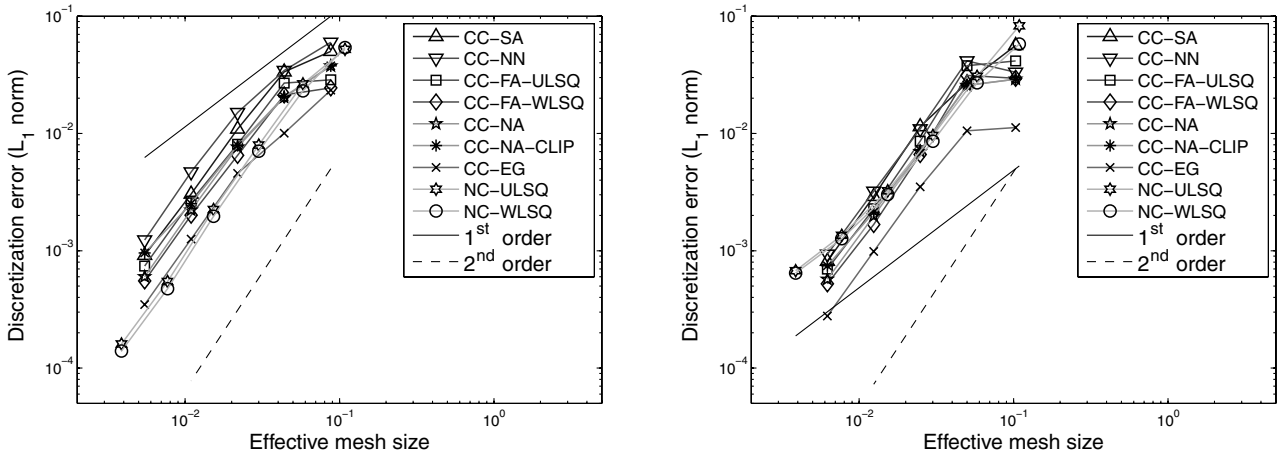

a) Grids of type (III_p) **b) Grids of type (IV_p)**

Fig. 7 Convergence of L_1 norms of discretization errors on isotropic irregular grids. Manufactured solution is $U = -\cos(2\pi x - \pi y)$. The convection direction is $\mathbf{a} = \left[\cos\left(\frac{7\pi}{16}\right), \sin\left(\frac{7\pi}{16}\right)\right]$.

C. Convergence of Discretization Errors

Discretization errors of all CC schemes, except the CC-NA-CLIP scheme, converge with second order on grids of all types, and the errors of the NC schemes converge with second order on grids of types (I)–(III), (II_p), and (III_p). As predicted in [4,7], discretization errors of NC schemes on perturbed quadrilateral and mixed-element grids converge with first order. The reason for this convergence degradation is the edge-based flux integration scheme, which is second-order accurate on simplex (triangular and tetrahedral) grids but only first-order accurate on perturbed quadrilateral and general mixed-element grids.

Figure 7 shows convergence of the L_1 norms of discretization errors for the manufactured solution $U = -\cos(2\pi x - \pi y)$ on grids of types (III_p) and (IV_p). The convection direction is $\mathbf{a} = [\cos(\frac{7\pi}{16}, \sin(\frac{7\pi}{16}))]$. The deviations of discretization errors observed in stochastic runs on grids with the same number of nodes are very small, so the error bounds are not shown. Although barely discernible, convergence of the discretization errors of the CC-NA-CLIP scheme deteriorates on finer grids. Detailed tests performed on finer grids and reported in Appendix A show that the discretization error convergence deteriorates to first order. Although not shown, the convergence of the L_∞ norms of the CC-NA-CLIP scheme exhibits signs of deterioration on coarser grids. For other schemes, convergence slopes are the same for all norms and do not change on finer grids.

The second-order discretization errors differ by less than an order of magnitude at a given effective mesh size. For reference, Figs. 7a and 7b include the convergence plots of discretization errors computed with the CC-EG scheme that uses gradients evaluated at each cell from the manufactured solution. The CC-EG plots represent the best possible second-order convergence, which can be achieved with a second-order CC formulation on given grids. Close proximity of the actual and the ideal second-order discretization errors indicates that the accuracy of the tested schemes is nearly optimal.

D. Convergence of Defect-Correction Iterations

On grids of type (I), the NC schemes and the CC-NN scheme correspond to the Fromm discretization of convection equation (1). A detailed study of DCI for the Fromm discretization on Cartesian grids has been reported in [16]. The study concludes that the error evolution can be divided into three stages: initial convergence, transition, and asymptotic convergence. Initial convergence is typically fast for random initial solutions; the transition convergence slows down, and the asymptotic convergence is fast again. The number of iterations within the transition region can grow slightly on finer grids. Asymptotic convergence rates do not deteriorate on finer grids. Convergence of DCIs on representative isotropic grids of types (III_p) and (IV_p) with 65^2 nodes is illustrated in Fig. 8. Convergence plots follow the pattern predicted in [16].

Asymptotic convergence rates on grids of each type is systematically studied by performing stochastic tests on 17^2 grids generated on the unit square. The spectral radius of the DCI matrix serves as the estimate of the asymptotic convergence rate. The spectral radius is computed on 32 independently generated grids for 32 representative flow directions. The following conclusions have been reached: DCIs converge fast for all schemes on unperturbed grids of types (I)–(IV) and on perturbed quadrilateral grids of type (I_p). The asymptotic rates for the CC-FA-ULSQ, CC-FA-WLSQ, CC-SA, CC-NA, and CC-NA-CLIP schemes are fast (better than 0.4) on all grids, independent of grid type. The asymptotic rates for the NC-ULSQ and NC-WLSQ schemes are around 0.5. Note that reported problems with the stability of DCIs for the NC-WLSQ schemes [17] and for the CC-NA scheme without clipping [8] are not observed on these isotropic grids.

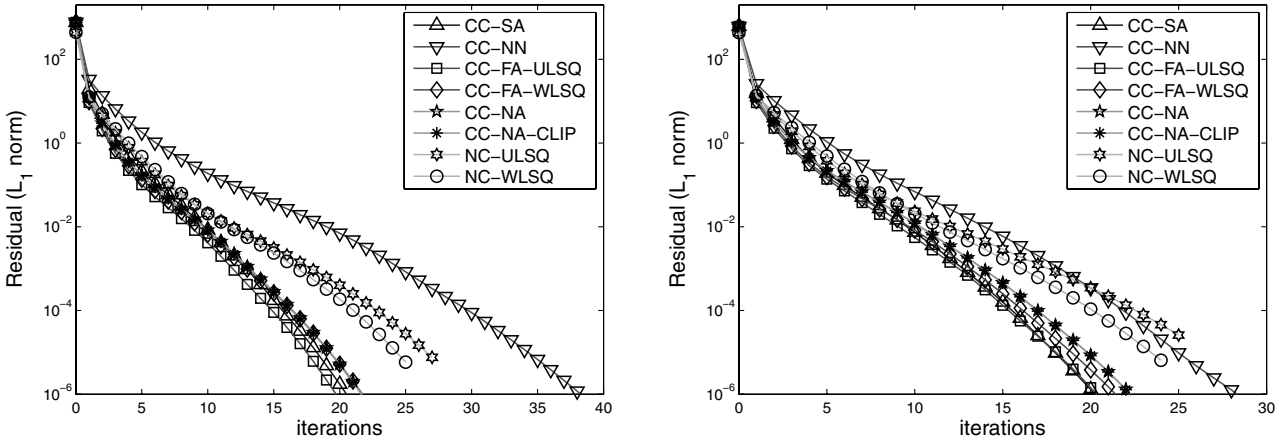

a) Grids of type (III_p) b) Grids of type (IV_p)

Fig. 8 DCI convergence on isotropic irregular grids. The convection direction is $\mathbf{a} = \left[\cos\left(\frac{7\pi}{16}\right), \sin\left(\frac{7\pi}{16}\right)\right]$.

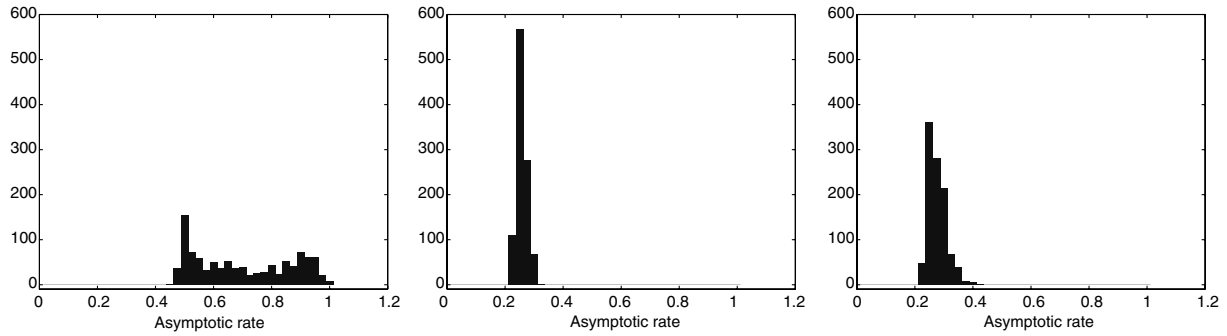

a) CC-NN scheme b) CC-FA-ULSQ scheme c) CC-SA scheme

Fig. 9 Distribution of spectral radius of the DCI matrix observed in 1024 stochastic tests on 17^2 isotropic grids of type (III_p).

The DCIs may diverge for the CC-NN scheme on grids of type (III_p) and (IV_p). The CC-NN convergence rate is strongly dependent on a specific combination of local grid geometry and flow direction; many stochastic tests are required to observe divergence in actual computations. Figure 9 shows the histograms of the spectral radius on grids of type (III_p) for the CC-NN, CC-FA-ULSQ, and CC-SA schemes. The spectral radii of the CC-FA-ULSQ and CC-SA schemes are small for all cases. The spectral radii of the CC-NN scheme are much larger. CC-NN spectral radii larger than 0.9 have been observed in 171 of the 1024 stochastic tests; one divergence case (a spectral radius larger than one) has occurred.

VII. Class (B): Anisotropic Grids in Rectangular Geometry

A. Grid Specification

In this section, FVD schemes are studied on stretched grids generated on rectangular domains. Figure 10 shows an example grid of type (III_p) with the maximal aspect ratio $\mathcal{A} = 10^3$. A sequence of consistently refined stretched grids is generated on the rectangle $(x, y \in [0, 1] \times [0, 0.5])$ in the following three steps:

1) A background regular rectangular grid with $N = (N_x + 1 \times (N_y + 1))$ nodes and a uniform horizontal mesh spacing $h_x = 1/N_x$ is stretched in the vertical direction toward the horizontal line $y = 0.25$. The y coordinates of the horizontal grid lines in the top half of the domain are defined as

$$y_{N_y/2+1} = 0.25; \qquad y_j = y_{j-1} + \hat{h}_y \beta^{j-[(N_y/2+1)]}, \quad j = \frac{N_y}{2} + 2, \ldots, N_y, N_y + 1 \tag{17}$$

Here, $\hat{h}_y = h_x/A$ is the minimal vertical mesh spacing; $\mathcal{A} = 10^3$ is a fixed maximal aspect ratio; and β is a stretching factor, which is found from the condition $y_{N_y+1} = 0.5$. The stretching in the bottom half of the domain is defined analogously.

2) Irregularities are introduced by random shifts of interior nodes in the vertical and horizontal directions. The vertical shift is defined as $\Delta y_j = \frac{1}{4}\rho \min\left(h_y^{j-1}, h_y^j\right)$, where ρ is a random number between -1 and 1, and h_y^{j-1} and h_y^j are vertical mesh spacings on the background stretched mesh around the grid node. The horizontal shift is introduced analogously, $\Delta x_i = \frac{1}{4}\rho h_x$. With these random node perturbations, all perturbed quadrilateral cells are convex.

3) Each perturbed quadrilateral is randomly triangulated (or not triangulated), depending on the grid type.

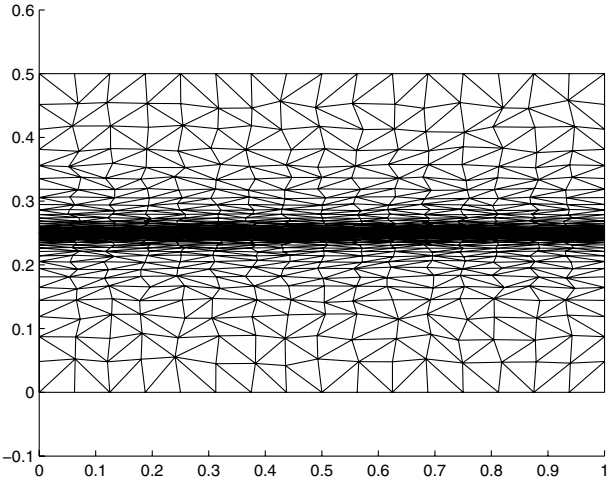

Fig. 10 Perturbed random triangular stretched grid with 17 × 65 nodes.

B. Gradient Reconstruction Accuracy

A recent study [18] assessed the accuracy of gradient approximations on various irregular grids with a high aspect ratio $\mathcal{A} = h_x/h_y \gg 1$. The study indicates that, for rectangular geometries and functions predominantly varying in the direction of small mesh spacing (y direction here), gradient reconstruction is accurate, providing small relative error converging with at least first order in consistent refinement on grids of all types. For manufactured solutions significantly varying in the direction of larger mesh spacing (x direction), the gradient reconstruction may produce extremely large $O(\mathcal{A}h_x)$ relative errors affecting the accuracy of the y-directional gradient component. Figure 11 shows examples of first-order-accurate gradient approximations that exhibit large relative errors on high-aspect-ratio grids of type (III).

Evaluation of gradient reconstruction accuracy is performed with the methodology of downscaling [4,7]. The computational tests are performed on a sequence of downscaled narrow domains $L \times (L/\mathcal{A})$ centered at the focal point $(x, y = (0.3, 0.5))$. The scale L changes as $L = 2^{-n}, n = 0, \ldots, 8$, and the considered aspect ratios are $\mathcal{A} = 10^6$ and $\mathcal{A} = 10^3$; the latter corresponds to the highest aspect ratio observed at the central line of the stretched grid shown in Fig. 10. On each domain, an independent high-aspect-ratio random grid of type (III) with 9^2 nodes is generated. The grid aspect ratio is fixed as $\mathcal{A}$ on all scales. The gradient reconstruction accuracy is measured at the interior control volumes. The NC-WLSQ and CC-FA-WLSQ schemes provide accurate gradients independent of the aspect ratio $\mathcal{A}$; the relative errors of gradient reconstructions provided by all other tested schemes are several orders of magnitude larger and directly

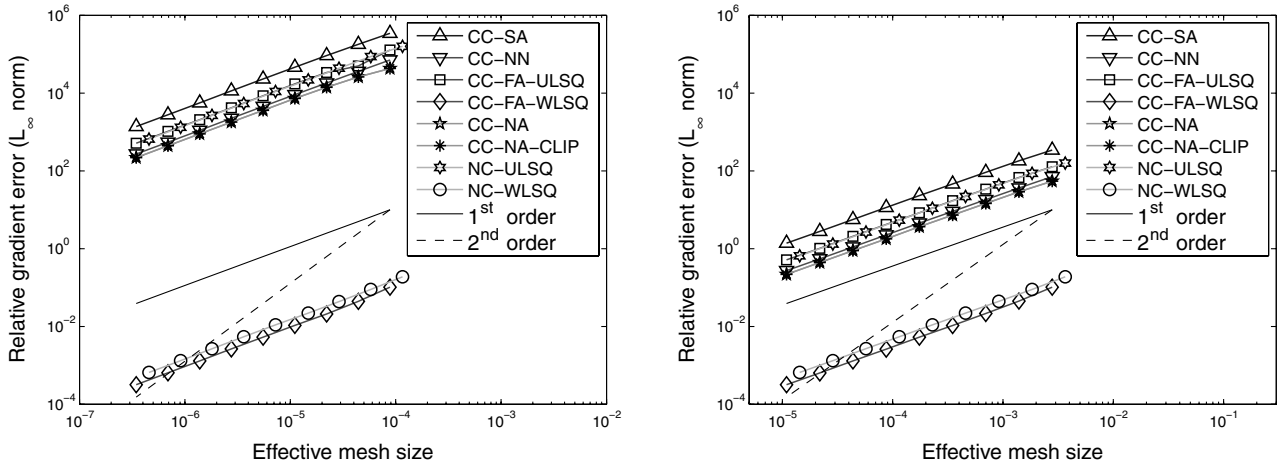

a) Aspect ratio $\mathcal{A} = 10^6$ **b) Aspect ratio $\mathcal{A} = 10^3$**

Fig. 11 Relative gradient errors for the manufactured solution $U = -\cos(2\pi x - \pi y)$ on anisotropic grids of type (III) downscaled toward the focal point $(x, y) = (0.3, 0.5)$.

Table 5 Relative error of gradient reconstruction on anisotropic irregular grids for solutions with a significant variation in the x direction of larger mesh spacing

	Grid types				
	(I)	(II)	(III)	(IV)	(I_p)–(IV_p)
NC-ULSQ	$O(h_x^2)$	$O(h_x^2)$	$O(\mathcal{A}h_x)$	$O(\mathcal{A}h_x)$	$O(\mathcal{A}h_x)$
NC-WLSQ	$O(h_x^2)$	$O(h_x^2)$	$O(h_x)$	$O(h_x)$	$O(\mathcal{A}h_x)$
CC-SA	$O(h_x^2)$	$O(h_x^2)$	$O(\mathcal{A}h_x)$	$O(\mathcal{A}h_x)$	$O(\mathcal{A}h_x)$
CC-NN	$O(h_x^2)$	$O(h_x^2)$	$O(\mathcal{A}h_x)$	$O(\mathcal{A}h_x)$	$O(\mathcal{A}h_x)$
CC-FA-ULSQ	$O(h_x^2)$	$O(h_x^2)$	$O(\mathcal{A}h_x)$	$O(\mathcal{A}h_x)$	$O(\mathcal{A}h_x)$
CC-FA-WLSQ	$O(h_x^2)$	$O(h_x^2)$	$O(h_x)$	$O(\mathcal{A}h_x)$	$O(\mathcal{A}h_x)$
CC-NA	$O(h_x^2)$	$O(h_x)$	$O(\mathcal{A}h_x)$	$O(\mathcal{A}h_x)$	$O(\mathcal{A}h_x)$

proportional to $\mathcal{A}$. All methods converge with first order in grid refinement.

A summary of the results concerned with gradient accuracy on anisotropic grids is presented in Table 5. Only the NC-WLSQ scheme provides gradient reconstruction accuracy on all unperturbed grids. All considered gradient reconstruction methods may generate large relative errors on perturbed grids of types (I_p)–(IV_p). The WLSQ method is ineffective on perturbed grids, because all stencil points can be essentially equidistant from the stencil center. Such situations occur more frequently for CC schemes. All CC schemes may generate large gradient errors, even on unperturbed mixed-element grids of type (IV). The CC-NN, CC-NA, and CC-FA-ULSQ methods may also have large relative errors on unperturbed random triangular grids of type (III); however, the CC-FA-WLSQ method always provides accurate gradients on these grids.

C. Convergence of Discretization Errors

A poor gradient reconstruction accuracy does not necessarily imply large discretization errors, and accurate gradients do not guarantee small discretization errors. To illustrate these properties, Fig. 12 shows discretization and gradient errors observed in stochastic tests performed on stretched grids of type (III_p) with small random node perturbation. The perturbations are limited by $\frac{1}{4}h_y$ in each dimension, where h_y is the local vertical mesh spacing. The manufactured solution is $U = \sin(\pi x + 2\pi y)$. The convection direction is $\mathbf{a} = (1, 0)$. Figure 12a shows the L_∞ norm of discretizations errors for the NC-WLSQ and CC-FA-WLSQ schemes. For comparison, the L_∞ norms of discretization errors for the NC-ULSQ scheme and for the ideal CC scheme (CC-EG) using exact gradients evaluated from the manufactured solution are also shown. The plot symbols indicate the mean errors, and bars indicate the maximum and minimum errors observed on 10 grids independently generated for each scale. Figure 12b shows convergence of relative gradient errors on the same grids. In agreement with results collected in Table 5, the NC-WLSQ and CC-FA-WLSQ schemes on such grids reconstruct gradients with small relative errors; conversely, the relative gradient errors of the NC-ULSQ scheme are large.

The accurate solutions obtained with the NC-ULSQ scheme, in spite of large relative gradient errors, are explained by the nature of the errors. The $O(\mathcal{A}h_x)$ gradient errors may occur on high-aspect-ratio grids and affect the y-gradient component aligned with the direction of small mesh spacing. On such grids, the y coordinates of the flux-reconstruction locations differ from the y coordinate of the control-volume center by $O(h_y)$. Thus, the errors in flux reconstruction caused by the inaccurate y-gradient component are $O(\mathcal{A}h_x h_y = O(h_x^2))$, comparable with other errors occurring in the FVD scheme, and sufficient to enable the second-order convergence of discretization errors.

The large and erratic discretization errors of the NC-WLSQ and CC-FA-WLSQ schemes are explained by random occurrences of unstable patterns characteristic for FVD schemes with the WLSQ gradient reconstruction. With these patterns, the main-diagonal coefficients of the FVD scheme may become negative. This instability is analyzed in Appendix B. Note that some coarse grids

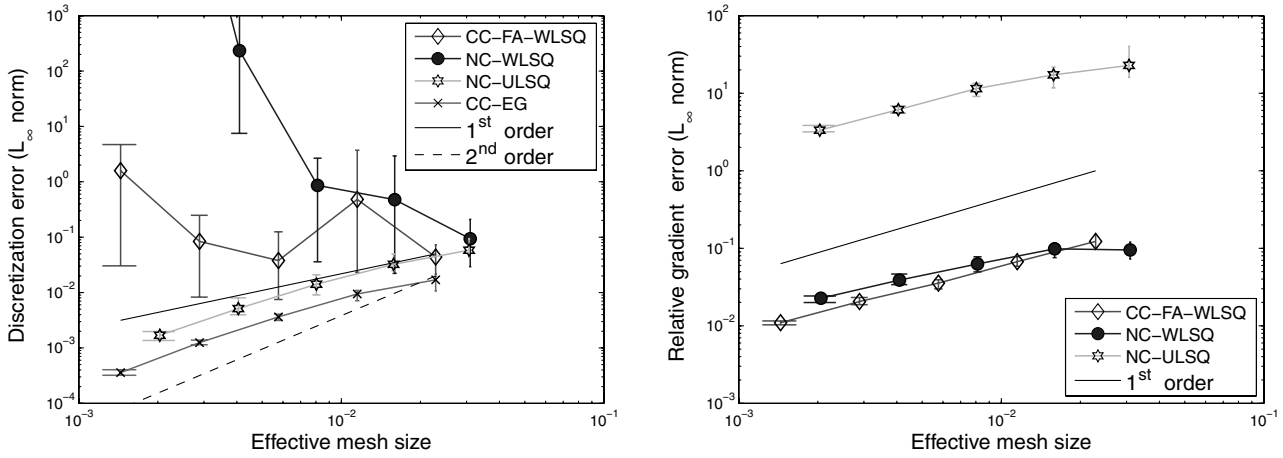

a) Discretization errors **b) Gradient errors**

Fig. 12 Convergence of discretization and gradient errors on stretched grids of type (III_p) with small node perturbations.

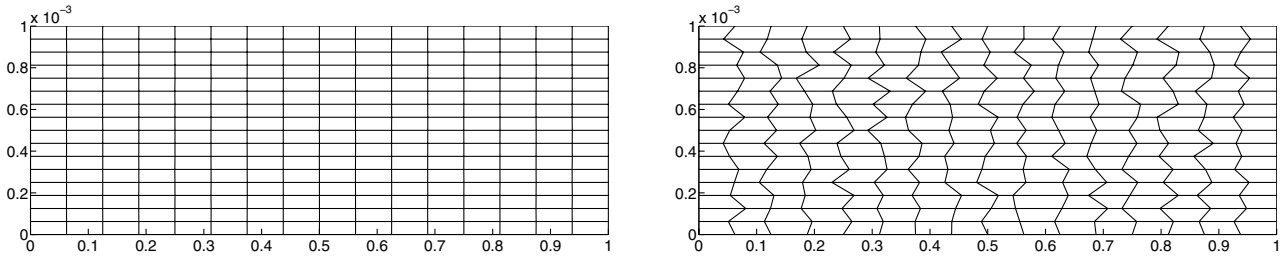

a) 1st family: small perturbations **b) 2nd family: large perturbations**

Fig. 13 Two 17^2 grids, with $\mathcal{A} = 1000$ representing families of grids of type (I_p) with small and large node perturbations.

may not contain unstable patterns, leading to discretization errors comparable with the errors of the NC-ULSQ and CC-EG schemes, and that the probability and severity of unstable patterns on the tested grids is lower for CC schemes.

To illustrate the effect of this instability on discretization errors in a simpler setting, stochastic tests have been performed for the NC-WLSQ scheme on a narrow domain $[0, 1] \times [0, 0.001]$ with the manufactured solution $U = \sin(\pi x + 2000\pi y)$. Two families of anisotropic ($\mathcal{A} \approx 1000$), irregular, quadrilateral grids are derived from Cartesian grids with 9^2, 17^2, 33^2, 65^2, and 129^2 nodes. First-family grids are derived by a small random shift of the x coordinate of each Cartesian-grid node, in the range of $2\rho h_y$, where $\rho \in [-1, 1]$ is a uniformly distributed random number. Second-family grids are derived by a larger shift of the x coordinate of each Cartesian-grid node, in the range of $\rho h_x/3$, and the random parameter ρ at vertically neighboring nodes is required to differ by at least 0.2. The latter requirement on the ρ variation is added to avoid occurrences of negative diagonal coefficients in the residual operator. Representative grids are shown in Figs. 13a and 13b. The grid from the first family appears unperturbed, while the grid of the second family is obviously strongly irregular. However, the grids of the first family are prone to negative main-diagonal coefficients.

The convergence of the L_1 norms of the discretization errors is shown in Fig. 14. The symbols indicate the mean errors, and bars indicate the maximum and minimum errors observed on ten grids independently generated for each scale. For the first grid family, the discretization errors do not decrease with grid refinement. In fact, the L_∞ norm of the errors is growing. For the second family, the discretization errors converge with first order in any norm, as expected for an edge-based NC scheme on irregular quadrilateral grids.

Second-order-accurate solutions have been previously reported [3,19] on grids with large gradient reconstruction errors. Here, similar results are observed for CC and NC FVD schemes for constant-coefficient convection. Convergence histories of the L_1 norms of discretization errors for the manufactured solution $U = \sin(\pi x + 2\pi y)$ on a sequence of consistently refined stretched grids of types (III_p) and (IV_p) are shown in Fig. 15. The convection direction is $\mathbf{a} = [\cos(\frac{7\pi}{16}, \sin(\frac{7\pi}{16}))]$. Grids with large node perturbations, specified in Sec. VII.A, are used. The tests have been performed stochastically, but only small deviations of the error norms have been observed on different grids of the same scale. Therefore, only one representative norm is shown.

On grids of type (III_p), all discretization errors converge with second order. Note that, from the convergence results reported in Appendix A, the discretization-error convergence order for the CC-NA-CLIP scheme is expected to deteriorate to first order on finer grids. The NC-ULSQ solutions converge with first order on grids of type (IV_p), as predicted [4,7]. Discretization errors of all CC schemes converge with second order and are close to each other and to the ideal discretization errors of the CC-EG scheme.

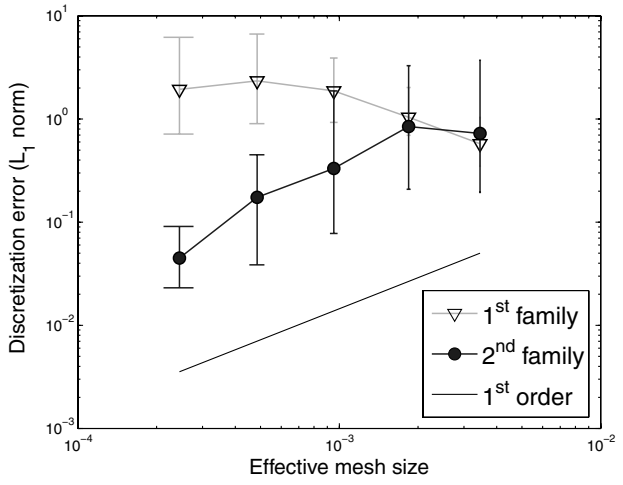

Fig. 14 Convergence of discretization errors for the NC-WLSQ scheme on two families of type (I_p) grids. Manufactured solution is $U = \sin(\pi x + 2000\pi y)$. The convection direction is $\mathbf{a} = (1, 0)$.

D. Convergence of Defect-Correction Iterations

Similar to the class (A) stochastic tests reported in Sec. VI, the DCI convergence on anisotropic grids is evaluated on 17^2 grids stochastically generated on a sequence of rectangular domains $[0, 1] \times [0, \frac{1}{\mathcal{A}}]$, with aspect ratios varying as $\mathcal{A} = 1, 10, 100$, and 1000. For each combination of scheme, grid type, and aspect ratio, the spectral radius of the DCI matrix is computed on 32 independently generated grids for 32 representative flow directions. The flow directions are horizontally inclined, with inclination angles (i.e., angles between the flow directions and the positive x direction) varying within the intervals $[-\frac{\pi}{2\mathcal{A}}, \frac{\pi}{2\mathcal{A}}]$ and $[\pi - \frac{\pi}{2\mathcal{A}}, \pi + \frac{\pi}{2\mathcal{A}}]$. This range of flow directions is chosen to expose the worst possible convergence rates. The rates observed for other flow directions are typically much better.

The following observations have been made: DCIs converge fast for all schemes on unperturbed grids of types (I)–(IV) and on perturbed quadrilateral grids of type (I_p). The asymptotic rates for the NC-ULSQ, CC-FA-ULSQ, CC-NA, and CC-NA-CLIP schemes are fast (0.5 or better) on all grids, independent of grid type and aspect ratio. The rates of the CC-SA scheme are somewhat slower (but still no worse than 0.8) on perturbed high-aspect-ratio grids of types (III_p)

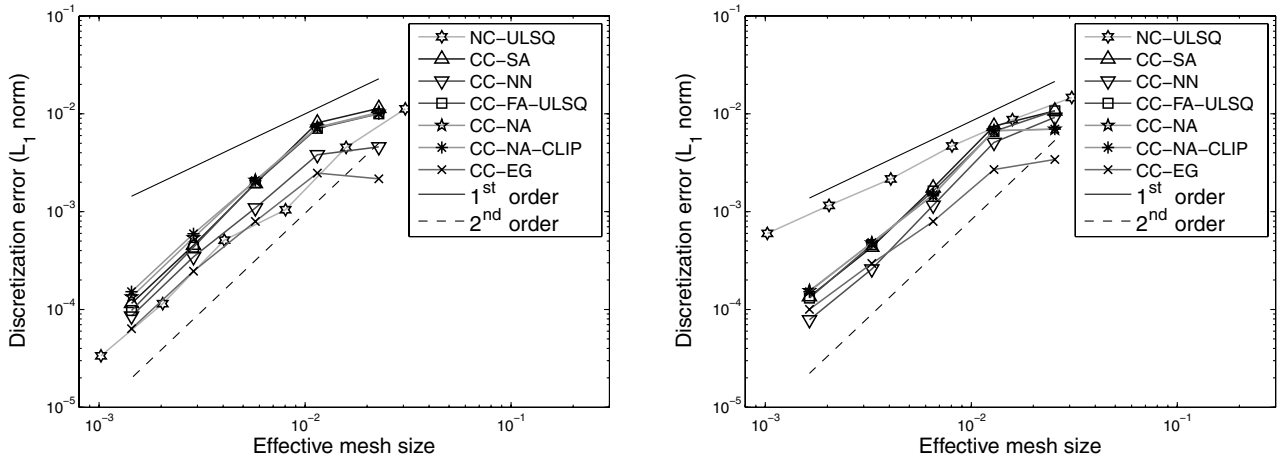

a) Grids of type (*IIIp*) **b) Grids of type (IV_p)**

Fig. 15 Convergence of discretization errors on irregular stretched grids for solution $U = \sin(\pi x + 2\pi y)$ and convection direction $\mathbf{a} = \left[\cos\left(\frac{7\pi}{16}\right), \sin\left(\frac{7\pi}{16}\right)\right]$.

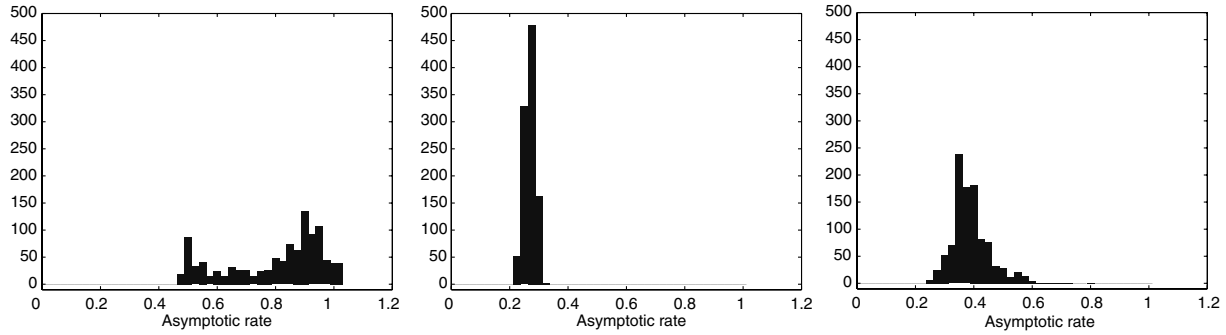

a) CC-NN scheme b) CC-FA-ULSQ scheme c) CC-SA scheme

Fig. 16 Distribution of spectral radius of DCI matrix observed in 1024 stochastic tests on 17^2 grids of type (III_p) with aspect ratio $A = 100$ and horizontally inclined flow directions.

and (IV_p). For certain combinations of local geometry and flow direction, DCIs for the CC-NN scheme may diverge on grids of types (III_p) and (IV_p). The iterations for the NC-WLSQ and CC-FA-WLSQ schemes diverge on high-aspect-ratio ($\mathcal{A} \geq 100$) grids of types (II_p), (III_p), and (IV_p). Somewhat surprisingly, for this rectangular geometry, the CC-NA scheme converges without clipping, even though the grids are highly irregular.

Figure 16 shows histograms of the spectral radius distributions for the CC-NN, CC-FA-ULSQ, and CC-SA schemes on grids of type (III_p) with an aspect ratio of $\mathcal{A} = 100$ and horizontally inclined flow directions. Many tests for the CC-NN scheme exhibit slow DCI convergence, and divergence has been observed in 13 (out of 1024) stochastic tests. The DCI convergence of the CC-FA-ULSQ scheme is always better than 0.33. For the CC-SA scheme, the largest observed DCI spectral radius is 0.8. Only seven tests showed the spectral radius larger than 0.6; only three of them showed the spectral radius larger than 0.7.

VIII. Class (C): Grids with Curvature and High Aspect Ratio

A. Grid Specification

In this section, we discuss FVD schemes on grids with curvature and high aspect ratio. The grid nodes are generated from a cylindrical mapping, where (r, θ) denote polar coordinates with spacings of h_r and h_θ, respectively. The grid aspect ratio is defined as the ratio of mesh sizes in the circumferential and the radial directions, $\mathcal{A} = Rh_\theta/h_r$, where R is the radius of curvature.

A measure of the curvature-induced mesh deformation is Γ, defined as

$$\Gamma = \frac{R[1 - \cos(h_\theta]h_r)}{} \approx \frac{Rh_\theta^2}{2h_r} = \mathcal{A}\frac{h_\theta}{2} \tag{18}$$

The following assumptions are made about the range of parameters: $R \approx 1$, $\mathcal{A} \gg 1$, and $\Gamma h_r \ll 1$, which implies that both h_r and h_θ are small. For a given value of $\mathcal{A}$, the parameter Γ may vary: $\Gamma \ll 1$ indicates meshes that are locally (almost) undeformed. As a practical matter, grids with $\Gamma < 0.2$ can be considered as nominally noncurved. In a mesh refinement that keeps $\mathcal{A}$ fixed, $\Gamma = O(\mathcal{A}h_\theta)$ asymptotes to zero. This property implies that on fine enough grids with a fixed curvature and aspect ratio, the discretization error convergence is expected to be the same as on similar grids generated on rectangular domains with no curvature.

Four basic types of 2-D grids are studied in the cylindrical geometry. Unlike the computational grids used in the rectangular geometry, random node perturbation is not applied to high-Γ grids, because even small perturbations in the circumferential direction may lead to nonphysical control volumes.

Computational grids used in the grid-refinement study are radially stretched grids with a radial extent of $1 \leq r \leq 1.2$ and an angular extent of 20° with a fixed maximal aspect ratio $\mathcal{A} \approx 1000$. The grids have four times more cells in the radial direction than in the circumferential direction. The maximum value of Γ changes approximately as $\Gamma \approx 22, 11, 5.5, \cdots$. The corresponding grid stretching ratios change as $\beta = 1.25, 1.11, 1.06, \cdots$. Representative grids of types (III) and (IV) are shown in Fig. 17.

B. Accuracy of Gradient Approximation

Our main interest is solutions varying predominantly in the radial direction on grids with $\Gamma \gg 1$, corresponding to meshes with large curvature-induced deformation. Computations and analyses reported earlier [17,19,20] concluded that the ULSQ gradient approximation is zeroth-order accurate for such solutions on grids with high Γ. The errors of gradient reconstruction for the manufactured solution $U = \sin(5\pi r)$ on high-Γ grids of types (I)–(IV) are summarized in Table 6. The approximate-mapping method described in Sec. III.C enables accurate gradient reconstruction. The NC-WLSQ and all AM schemes reconstruct accurate gradients on grids of all types. All other schemes show large $O(1)$ errors on mixed-element grids of type (IV). The CC-FA-WLSQ provides accurate gradient reconstruction on grids of type (III). Schemes using ULSQ gradient reconstruction in Cartesian coordinates produce large gradient errors, even on regular grids.

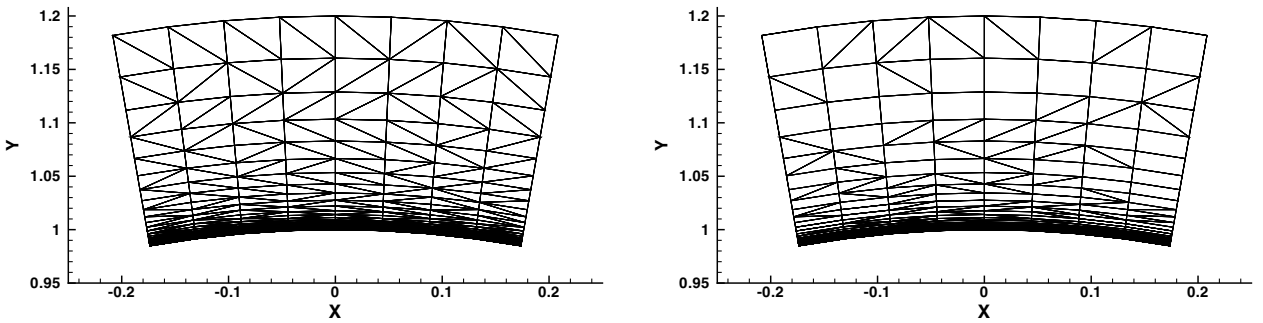

a) Grid of type (III) b) Grid of type (IV)

Fig. 17 Representative 9 × 33 irregular stretched high-Γ grids.

Table 6 High-Γ grids: relative errors of gradient reconstruction in global Cartesian coordinates[a]

	Grid Types			
	(I)	(II)	(III)	(IV)
NC-ULSQ	$O(1)$	$O(1)$	$O(1)$	$O(1)$
NC-WLSQ	$O(h_\theta^2)$	$O(h_\theta^2)$	$O(h_\theta)$	$O(h_\theta)$
NC-ULSQ-AM	$O(h_\theta^2)$	$O(h_\theta^2)$	$O(h_\theta)$	$O(h_\theta)$
CC-NN	$O(1)$	$O(1)$	$O(1)$	$O(1)$
CC-FA-ULSQ	$O(1)$	$O(1)$	$O(1)$	$O(1)$
CC-FA-WLSQ	$O(h_\theta^2)$	$O(h_\theta)$	$O(h_\theta)$	$O(1)$
CC-SA	$O(1)$	$O(1)$	$O(1)$	$O(1)$
CC-NA	$O(h_\theta^2)$	$O(h_\theta)$	$O(1)$	Degenerate
CC-NA-CLIP	$O(h_\theta)$	$O(h_\theta)$	$O(1)$	Degenerate
CC-NN-AM	$O(h_\theta^2)$	$O(h_\theta)$	$O(h_\theta)$	$O(h_\theta)$
CC-FA-ULSQ-AM	$O(h_\theta^2)$	$O(h_\theta)$	$O(h_\theta)$	$O(h_\theta)$
CC-SA-AM	$O(h_\theta^2)$	$O(h_\theta)$	$O(h_\theta)$	$O(h_\theta)$

[a]Manufactured solution is $U = \sin(5\pi r)$.

For illustration, Fig. 18 shows the relative accuracy of gradients reconstructed on grids of type (IV). The erratic convergence and large gradient errors of the CC-NA scheme are explained by NA degeneration on high-Γ mixed-element grids. On these grids, there are local geometries where the nodal solution is averaged from four neighboring cells. The four cell centers involved in such averaging may be located on a straight line, thus leading to degeneration. The sketch in Fig. 19 illustrates this phenomenon. The topology of the sketch (two quadrilaterals on top of two triangles) is identical to the topology causing the degradation on high-Γ mixed-element grids generated by the method of advancing layers. Note that such degradation cannot be realized on single-element [types (I), (II), or (III)] and/or low-Γ advancing-layer grids.

C. Discretization Error Convergence

Convergence of L_1 norms of discretization errors of FVD schemes, with and without approximate mapping, is shown in Fig. 20 for grids of type (III) and for the manufactured solution $U = \sin(5\pi r)$ and the convection direction $\mathbf{a} = [\cos(\frac{7\pi}{16}, \sin(\frac{7\pi}{16}))]$. All discretization errors converge with the second order. The level of discretization errors obtained by the schemes with $O(1)$ error in the gradient reconstruction is similar to the level obtained by the schemes with either approximate mapping or exact gradients. Indeed, an $O(1)$ error is associated only with the radial component of the gradient. If the face center location is shifted from the control-volume center in the purely radial direction, then the error in flux reconstruction is $O(h_r)$. If both circumferential and radial shifts are involved, then the radial shift is $O(\Gamma h_r = O(h_\theta^2))$ at most. On high-Γ grids, $h_r \ll h_\theta^2$. Therefore, the maximum error in the flux reconstruction is bounded by $O(h_\theta^2)$.

On unperturbed grids of types (I)–(IV), the level of discretization errors on grids with the same number of degrees of freedom varies significantly, depending on the locations of the data points with respect to the manufactured solution. This property is illustrated in Fig. 21, where the L_1 norms of discretization errors of the CC-NN-AM, CC-EG, and NC-ULSQ-AM schemes are shown for the stretched grids of type (I), horizontal convection, $\mathbf{a} = (1, 0)$, and three manufactured solutions. Excluding boundary effects, the number of degrees of freedom on grids of type (I) is the same for CC and NC formulations, but the locations of the data points are slightly different. The CC errors are close to each other on fine grids in all the tests. For $U = \sin(5\pi r)$, the errors of the NC-ULSQ-AM scheme are about four times smaller than CC errors; for $U = \sin(\pi r)$, all errors are about the same; and for $U = \sin(0.2\pi r)$, the CC errors are about two times smaller than the NC errors. Note that the differences between the CC and NC errors disappear on grids with no stretching. The large variations between CC and NC discretization errors

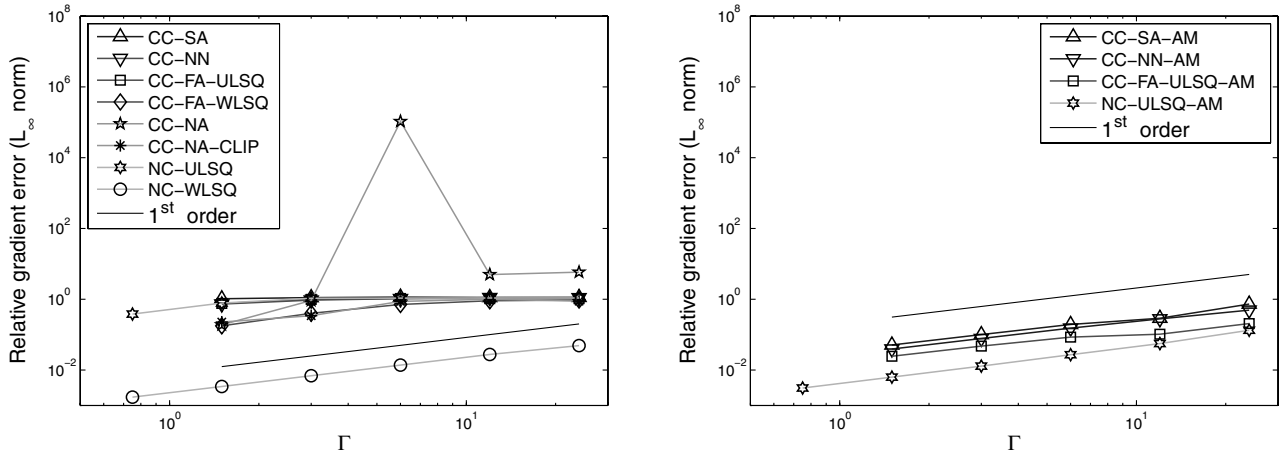

a) Cartesian *x*, *y* coordinates **b) Approximate mapping**

Fig. 18 Convergence of relative gradient errors on high-Γ stretched grids of type (IV) with a maximum aspect ratio of $\mathcal{A} = 1000$.

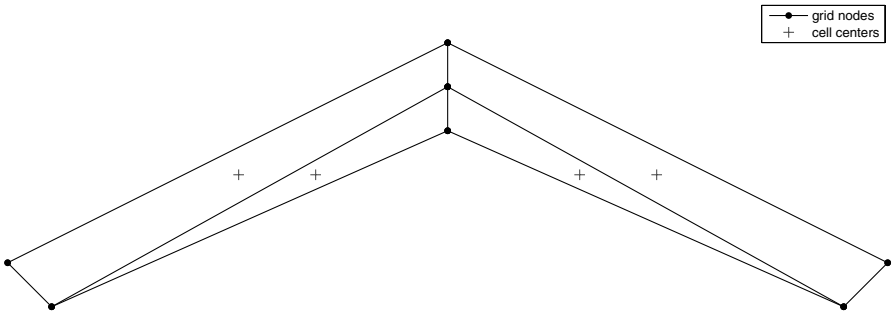

Fig. 19 Sketch of a grid leading to collinear cell centers and degradation of the NA procedure.

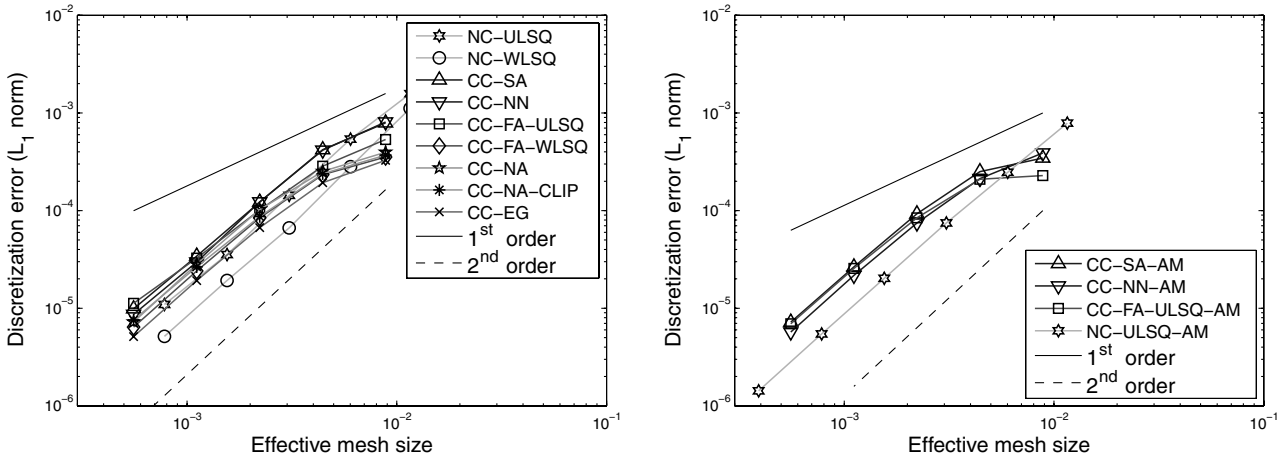

a) Cartesian coordinates **b) Approximate mapping**

Fig. 20 Convergence of discretization errors on high-Γ stretched grids of type (III) with a maximum aspect ratio of $\mathcal{A} = 1000$.

observed, even on mildly stretched grids of type (I), indicate significant accuracy gains that can be achieved with grid optimization. They also indicate that the conclusion that the discretization accuracies of good CC and NC schemes are similar on grids with similar degrees of freedom (such a conclusion would benefit CC schemes that typically provide more degrees of freedom on the same grids) is not straightforward for inviscid flows. To make such a conclusion, one should compare errors on optimized grids with the same number of degrees of freedom; the grid optimization should be done individually for each FVD scheme.

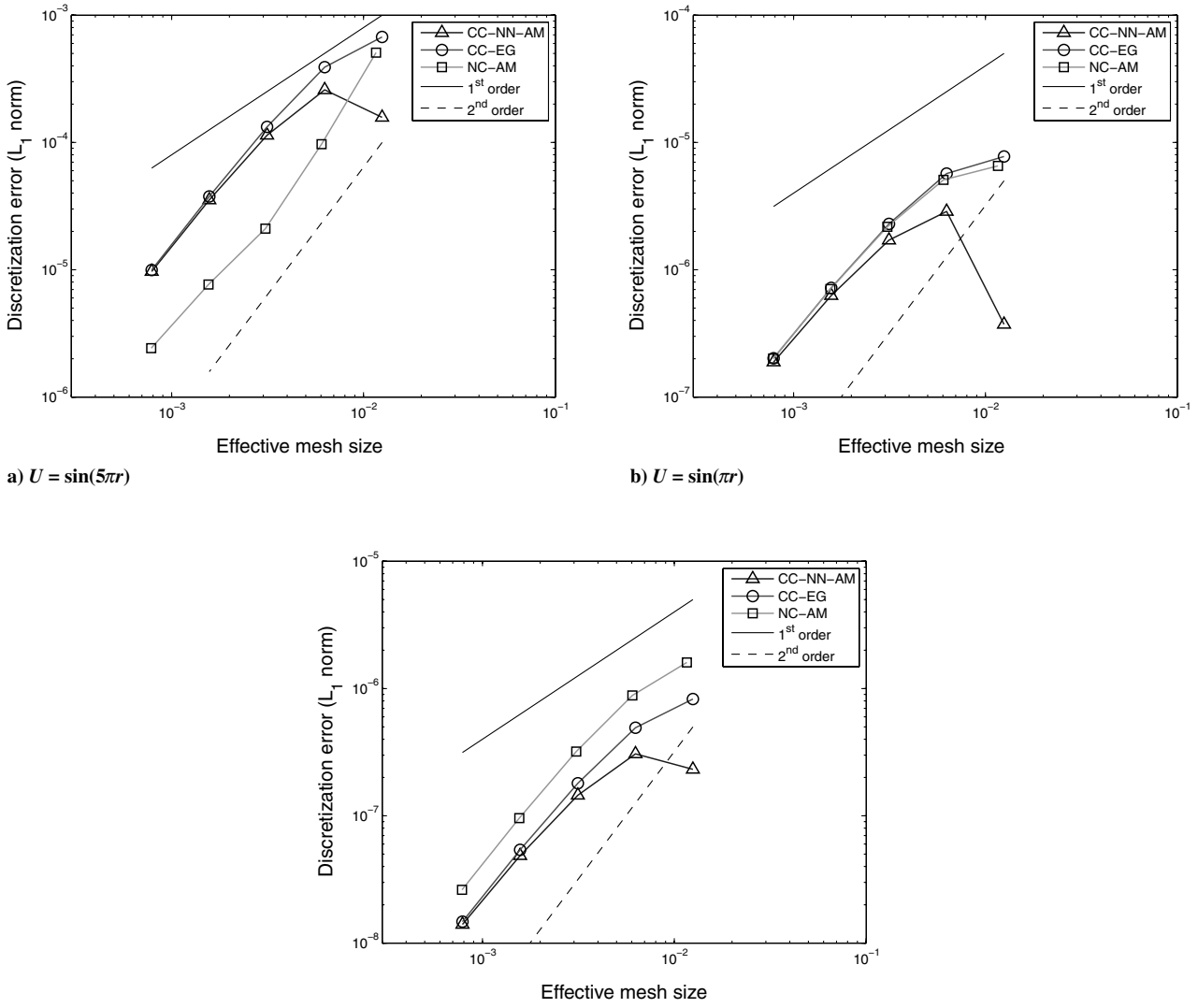

a) $U = \sin(5\pi r)$ **b)** $U = \sin(\pi r)$

c) $U = \sin(0.2\pi r)$

Fig. 21 Discretization errors for three manufactured solutions on stretched grids of type (I) with a maximum aspect ratio of $A = 1000$. The convection direction is $\mathbf{a} = (1, 0)$.

Table 7 Ranges of asymptotic convergence rates of DCI on anisotropic curved grids[a]

Γ	0.02	20
NC-ULSQ	0.43–0.48	0.8–0.98
NC-WLSQ	0.44–0.50	Diverge
NC-ULSQ-AM	0.43–0.47	0.49–0.58
CC-NN	0.45–0.52	0.13 (I), diverge (II, III, IV)
CC-FA-ULSQ	0.23–0.48	0.09–0.17
CC-FA-WLSQ	0.31–0.48	0.49 (I), diverge (II, III, IV)
CC-SA	0.26–0.48	0.11–0.18
CC-NA	0.24–0.48	Diverge
CC-NA-CLIP	0.24–0.48	0.94 (I, IV), 0.27–0.35 (II, III)
CC-NN-AM	0.45–0.52	0.45–0.52
CC-FA-ULSQ-AM	0.23–0.48	0.23–0.45
CC-SA-AM	0.23–0.48	0.32–0.48

[a]If no grid type is shown, the range describes convergence rates for grids of all types. Special cases are indicated by grid types in parentheses.

D. Convergence of Defect-Correction Iterations

DCI convergence rates on high-Γ grids are sensitive to the flow direction, improving for flows aligned with the radial direction of the strong anisotropy. In this section, the horizontal flow direction is chosen to expose the worst-case scenario. The tests are performed on computational domains, with the angular extent of 20° and the radial extent of $r \in [1, 1 + L]$, where $L = 0.2, 0.02, 0.002$, and 0.0002. The grids with 17^2 nodes correspond to $\Gamma \approx 0.02$, 0.2, 2, and 20. The asymptotic convergence rates are computed as the spectral radius of the corresponding DCI matrices and then confirmed in actual tests. On irregular grids of types (III) and (IV), the tests are performed stochastically. For each scheme and grid type, the DCI spectral radius is computed for 30 independently generated grids.

Ranges of DCI convergence rates on grids of various types with $\Gamma = 0.02$ and $\Gamma = 20$ are shown in Table 7. DCIs converge well for all schemes on low-Γ grids. On high-Γ grids, DCI divergence has been observed for the NC-WLSQ and CC-NA schemes on grids of all types. For the CC-NN and CC-FA-WLSQ schemes, divergence has been observed on grids of types (II), (III), and (IV). DCIs for the NC-ULSQ scheme converge slowly. Clipping was originally introduced to stabilize convergence of the CC-NA scheme, and DCIs for the CC-NA-CLIP scheme converge for all grids considered, demonstrating fast rates on triangular grids of types (II) and (III). DCI convergence dramatically improves for schemes with approximate mapping; DCIs for the NC-ULSQ-AM and CC-NN-AM scheme converge much better than their unmapped counterparts on the same grids. Overall, DCI convergence rates are fast for the CC-SA, CC-FA-ULSQ, and all approximate-mapping schemes on grids of all types; for the CC-NA-CLIP scheme on grids of types (II) and (III); and for the CC-NN and CC-FA-WLSQ schemes on grids of type (I).

The DCI behavior can be analyzed in a very simple setting. For example, DCI convergence for NC FVD schemes can be considered for a pair of interior grid nodes under the assumption that solutions in all surrounding nodes are overspecified. Representative interior grids of type (I) and type (II) are sketched in Fig. 22. DCIs have been analyzed on sequences of grids corresponding to various values of Γ with fixed circumferential mesh spacing and varying radial mesh spacing. For simplicity, convection with the unit horizontal velocity is assumed.

The variations of the spectral radius of the DCI matrix are shown in Fig. 23. On high-Γ grids of both types, DCIs diverge for the NC-WLSQ scheme, converge slowly for the NC-ULSQ scheme, and converge fast for the NC-ULSQ-AM scheme. The DCIs are unstable for the NC-WLSQ scheme on type (I) meshes, even though the

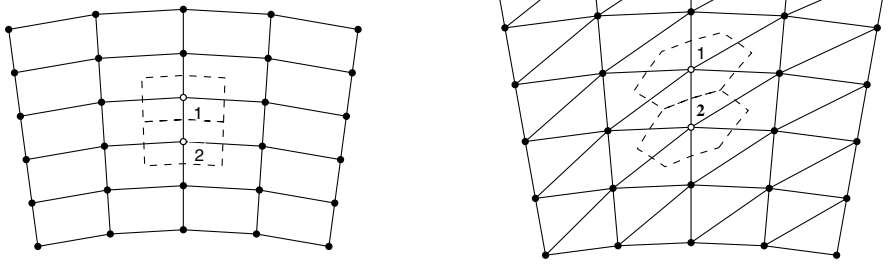

a) Grid of type (I) b) Grid of type (II)

Fig. 22 Sketch of interior grids of class (C). The unknown solutions are at nodes 1 and 2. Black bullets indicate nodes with overspecified solutions, and dashed lines indicate control volumes around nodes 1 and 2.

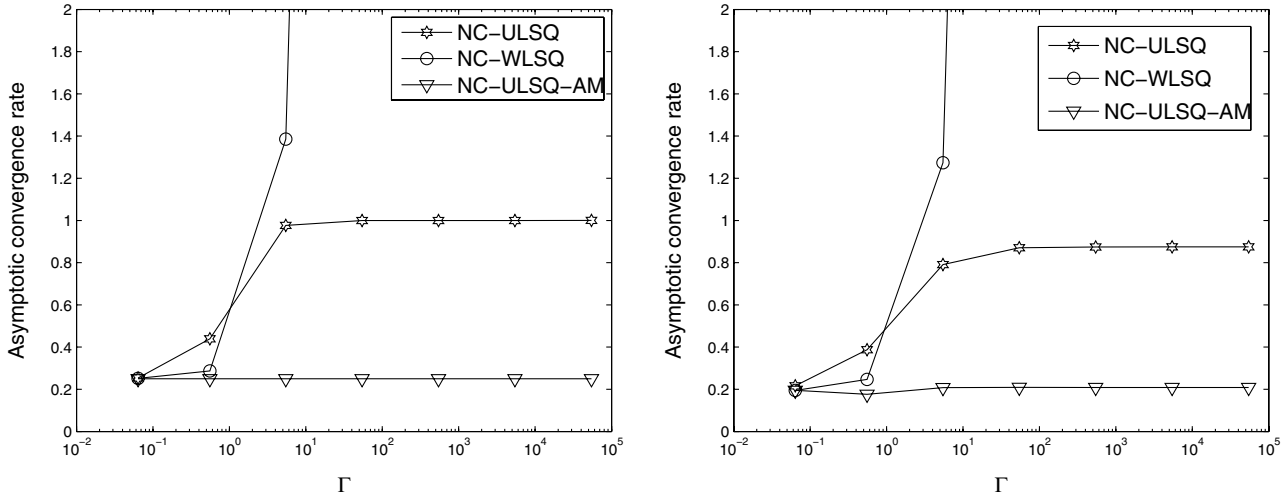

a) Grid of type (I) b) Grid of type (II)

Fig. 23 Asymptotic convergence rates for NC schemes.

coefficients of NC-WLSQ gradient reconstruction are very nearly the same as the coefficients of the NC-ULSQ-AM gradient reconstruction. The main cause of the divergence is the interior-state interpolation in the nearly circumferential-edge directions. On high-Γ grids, the radial coordinates of the edge midpoints are displaced by $O(\Gamma h_r)$ from the nodes. Within the simple setting of a type (I) grid (Fig. 22a), such displacement results in offdiagonal terms in the target scheme that are larger than the diagonal terms. In contrast, the driver scheme has zero offdiagonal terms. Although not shown, DCIs exhibit fast convergence for the target NC operator, constructed using either WLSQ or ULSQ gradients and approximate-mapping interior-state interpolations. Thus, the improvements in DCI with the mapping technique accrue mainly through the state-variable interpolations.

IX. Conclusions

Two node-centered and six cell-centered schemes have been compared for finite volume discretization of a constant-coefficient convection equation as a model of inviscid flow terms. All schemes are nominally second-order accurate and use either weighted or unweighted least-squares minimization. The schemes have been compared for complexity, accuracy, and convergence rates of defect-correction iterations with a first-order driver. The cell-centered nearest-neighbor scheme has the lowest complexity; in particular, its stencil involves the least number of neighbors. A version of the scheme that involves smart augmentation of the least-squares stencil has only a moderate complexity increase. All other schemes have larger complexity; the complexity of node-centered schemes is lower than the complexity of cell-centered schemes with node averaging or with full augmentation of the least-squares stencil.

Comparisons of accuracy and convergence rates of defect-correction iterations have been made for three grid classes: class (A) includes isotropic grids in a rectangular geometry, class (B) includes anisotropic grids representative of adaptive-grid simulations, and class (C) includes anisotropic advancing-layer grids representative of high-Reynolds-number turbulent-flow simulations over a curved body. Regular and irregular grids are considered, including mixed-element grids and grids with random perturbations of nodes. Computations on irregular grids have been performed stochastically. All tests have been performed on consistently refined grids for smooth manufactured solutions.

For the tests on grids of class (A), the following observations have been made. The cell-centered node-averaging scheme with clipping fails to approximate gradients and degrades solution accuracy to the first order. As expected, the node-centered discretization errors converge with second order on triangular and regular quadrilateral grids and with first order on mixed-element and perturbed quadrilateral grids. Second-order discretization errors are quantitatively similar on grids with the same degrees of freedom and closely approach ideal second-order errors exhibited by the cell-centered scheme with exact gradients. The defect-correction iterations may diverge for the cell-centered nearest-neighbor scheme on perturbed grids with random triangular elements.

For the tests on grids of class (B), all schemes may produce $O(\mathcal{A}h_x)$ large relative errors in gradient reconstruction on perturbed grids; here, $\mathcal{A}$ is the grid aspect ratio and h_x is the larger mesh spacing. Discretization errors of the schemes with weighted least-squares gradient reconstruction diverge in grid refinement on grids with small perturbations. For all other schemes, the errors converge with second order and closely approach the ideal second-order errors computed with exact-gradient reconstruction. Defect-correction iterations may diverge for the weighted east-squares schemes and for the cell-centered nearest-neighbor scheme and converge fast for all other schemes.

On grids of class (C), the range of grid parameters has been chosen to enforce significant curvature-induced grid deformations, characterized by the large values of the parameter Γ. All tests have been performed for manufactured solutions smoothly varying in the radial direction only. Accurate gradients are reconstructed on all grids by the least-squares minimizations performed in local approximate-mapping coordinates and by the node-centered weighted least-squares scheme. All other schemes generate $O(1)$ errors in gradient reconstruction on at least some grids. The node-averaging schemes may degenerate on mixed-element grids. All other schemes provide second-order discretization errors. Consistent with previous observations, defect-correction iterations may diverge for the weighted least-squares schemes and for the cell-centered node-averaging and nearest-neighbor schemes. The asymptotic convergence for the node-centered unweighted least-squares scheme is slow and may stagnate. Convergence rates of defect-correction iterations for the approximate-mapping schemes and for the cell-centered smart-augmentation and full-augmentation schemes are fast on all grids. Overall, the cell-centered smart-augmentation scheme is the most attractive; it offers low complexity, accuracy comparable with that of the exact-gradient scheme, and fast convergence of defect-correction iterations on all grids. The cell-centered nearest-neighbor approximate-mapping scheme is a good choice for discretization within boundary layers on high-aspect-ratio grids generated by the advancing-layer method. The node-centered unweighted least-squares approximate-mapping scheme presents the best node-centered option.

Several other observations have been made in the course of this work:

1) Smoothness of grid metrics, such as volume and face area, is often used as a grid quality measure, implying that a better accuracy can be achieved on grids with smoother metrics. The examples in the paper showed that, with robust discretization schemes, accurate solutions can be achieved on grids with discontinuous metrics. Moreover, metrics smoothness may be misleading when considered in isolation from specific schemes. In particular, it was shown that the discretization accuracy of the node-centered weighted least-squares scheme is much better on strongly irregular grids with discontinuous metrics than on certain almost-regular grids with minimal metric perturbations.

2) On high-aspect-ratio grids, gradient reconstruction accuracy is neither necessary nor sufficient for obtaining design-order discretization errors. Indeed, schemes with large relative errors in gradient reconstruction provided discretization errors comparable with the errors of the exact-gradient scheme. This phenomenon is explained by the specific nature of the gradient errors introduced on high-aspect-ratio grids that typically affect only certain gradient components and result in flux-reconstruction errors that are small enough to enable second-order convergence of discretization errors. On the other hand, the weighted least-squares reconstruction provides locally accurate gradients, but the obtained schemes may lose stability and accuracy. Note, however, that gradient accuracy is expected to be critical for discretizations involving gradient sources, entropy fixes, and/or gradient-based limiters.

3) In many tests, the observed discretization errors were similar on grids with similar degrees of freedom. However, some tests performed on stretched quadrilateral grids that provide similar degrees of freedom for both cell-centered and node-centered formulations showed large variations in discretization errors. These variations have been traced to slight differences in the locations of the degrees of freedom with respect to the manufactured solutions. This sensitivity indicates that there is a large potential accuracy gain that can be achieved by grid optimization. On the other hand, the conclusion about the true relationship between the discretization errors and degrees of freedom cannot be drawn from the tests performed on the nonoptimized grids considered in this paper.

Appendix A: Effects of Clipping

The isotropic grid tests reported in this appendix are performed for the CC-NA and CC-NA-CLIP schemes and demonstrate the detrimental effects of clipping on the convergence of gradient and discretization errors in grid refinement. Irregular triangular grids of type (III_p) are considered. These grids are characterized by a higher percentage of clipped nodes; about 10% of the interior nodes are clipped. Figure A1a shows an example of a grid of type (III_p) with 17^2 nodes; nodes where clipping occurs are circled.

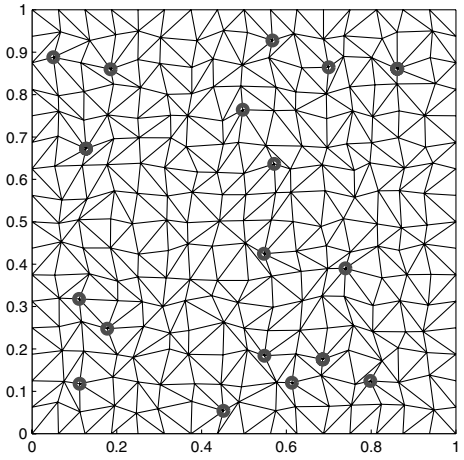

a) Random triangular grid with 17^2 nodes

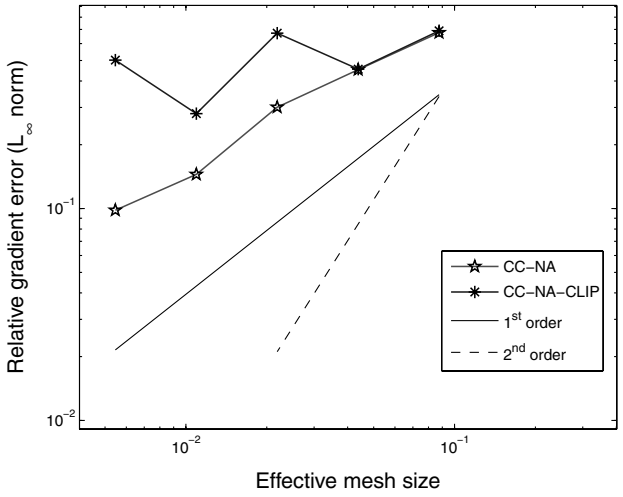

b) Gradient errors

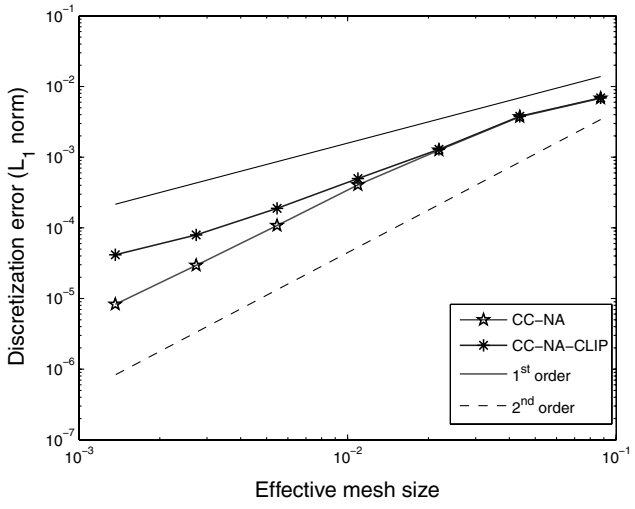

c) Discretization errors

Fig. A1 Accuracy of CC-NA schemes on isotropic, irregular, and triangular grids of type ($\mathbf{III}_p$). Manufactured solution is $U = -\cos(2\pi x - \pi y)$.

Figure A1b shows that the gradients reconstructed by the CC-NA-CLIP scheme do not approximate the exact gradients. The CC-NA scheme provides a first-order-accurate gradient reconstruction, which is sufficient for second-order discretization accuracy. Figure A1c presents the convergence of the L_1 norms of discretization errors. The CC-NA scheme demonstrates second-order convergence of discretization errors, which is consistent with results reported by Mitchell [21] for Ringleb flow. The discretization error convergence of the CC-NA-CLIP scheme exhibits second order on the coarse grids, but then it degrades to first order. Although not shown, the L_∞ norm of discretization errors of the CC-NA-CLIP scheme shows degradation on coarser grids in grid refinement. Asymptotically, L_∞ norms of both NA schemes converge with the same orders as the corresponding L_1 norms. Note that, on grids with a smaller percentage of clipped nodes, convergence degradation becomes visible only on finer grids. This may explain why such degradation has not been reported for practical computations.

Appendix B: Instability of Weighted Least-Squares Schemes on Grids with Small Perturbations

As shown in Secs. VII and VIII, WLSQ methods improve gradient reconstruction accuracy on high-aspect-ratio unperturbed grids of types (I)–(IV). These grids have well-defined lines aligned with the direction of strong anisotropy. The analysis presented in this section shows that FVD schemes using the WLSQ gradient reconstruction become unstable with small perturbations of this grid alignment. This instability manifests itself in the appearance of large negative coefficients on the main diagonal of the residual operator. As a result, DCIs diverge and discretization errors behave erratically in grid refinement.

For illustration, we consider the NC-WLSQ scheme on a quadrilateral grid with a uniformly high aspect ratio $\mathcal{A} = h_x/h_y$, where h_x and h_y are horizontal and vertical mesh sizes, respectively. Small periodic perturbations are introduced to every other node on every second horizontal line; the nodes are shifted left by a distance of $\bar{s}$. A sketch of a perturbed grid is shown in Fig. B1. The goal of the analysis is to compute the contribution to the residual at node 0 from the solution at the same node: the main-diagonal coefficient of the residual operator. For simplicity, the convection velocity is taken as $\mathbf{a} = (1, 0)$.

First, gradients at nodes 0 and 1 are reconstructed with the WLSQ method. For node 0, assuming the node is at the origin, the coordinates x_k and y_k of all stencil nodes are given in Table B1, where the subindex is a node indicator.

The linear reconstruction $U^r(x, y)$ of a general function $U(x, y)$ over the control volume around node 0 is defined as

$$U^r \equiv U_0 + ax + by \tag{B1}$$

where $U_0 = U(0,0)$. The components of the reconstructed gradient, $\nabla_r U = (a, b^T)$, are found by minimizing the sum of the squares of the (weighted) differences between the actual function and the linear fit at the stencil points:

$$\sum_k [\mu_k (U_k^r - U_k]^2 \to \min) \tag{B2}$$

where μ_k are weights:

$$\mu_k = \frac{1}{\sqrt{x_k^2 + y_k^2}} \tag{B3}$$

The gradient reconstructed at node 0 is

$$a_0 = \frac{1}{2}\frac{h_y^2 + \bar{s}^2}{h_y^2 + 2\bar{s}^2}\left[U_5 \frac{1}{h_x + \bar{s}} - U_1 \frac{1}{h_x - \bar{s}} + \left(U_4 + U_6 - 2U_0 \frac{\bar{s}}{h_y^2 + \bar{s}^2} + U_0\left(\frac{1}{h_x - \bar{s}} - \frac{1}{h_x + \bar{s}}\right)\right)\right], \qquad b_0 = \frac{1}{2h_y}[U_4 - U_6]\Big) \tag{B4}$$

Analogously, the gradient reconstructed at node 1 is

$$\begin{aligned} a_1 &= \frac{1}{2}\left[U_0 \frac{1}{h_x - \bar{s}} - U_2 \frac{1}{h_x + \bar{s}} - U_1 \frac{2\bar{s}}{h_x^2 - \bar{s}^2}\right], \\ b_1 &= \frac{1}{2h_y}[U_3 - U_7] \end{aligned} \tag{B5}$$

For the chosen convection direction, the FVD residual operator on the control volume around node 0 is formed as

$$\frac{h_y}{V}\left[\left(U_0 + a_0 \frac{h_x + \bar{s}}{2}\right) - \left(U_1 + a_1 \frac{h_x - \bar{s}}{2}\right)\right] \tag{B6}$$

where $V = h_x h_y$. The coefficient of U_0 is

$$\frac{1}{h_x}\left[\frac{3}{4} - \frac{1}{2}\frac{\bar{s}h_x}{h_y^2 + 2\bar{s}^2} - \frac{1}{2}\frac{\bar{s}^2}{h_y^2 + 2\bar{s}^2} + \frac{1}{2}\frac{h_y^2 + \bar{s}^2}{h_y^2 + 2\bar{s}^2}\frac{\bar{s}}{h_x - \bar{s}}\right] \tag{B7}$$

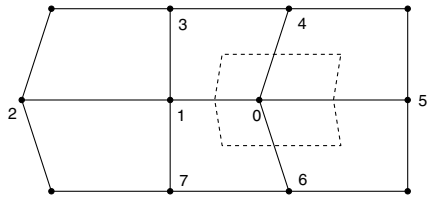

Fig. B1 Sketch of perturbed grid; dashed line indicates control volume around node 0.

Table B1 Coordinates of stencil points for gradient reconstruction at node 0

k	x_k	y_k
0	0	0
1	$-h_x + \bar{s}$	0
4	$\bar{s}$	h_y
5	$h_x + \bar{s}$	0
6	$\bar{s}$	$-h_y$

Assuming $\mathcal{A} \gg 1$ and $0 < \bar{s} \ll h_x$, the last term in the brackets is negligibly small compared with the other terms and may be ignored. In particular, if $\bar{s} = h_y$, the leading part of the coefficient would be

$$\frac{1}{h_x}\left[\frac{7}{12} - \frac{\mathcal{A}}{6}\right] \tag{B8}$$

which is a large negative number on grids with a high aspect ratio. All WLSQ schemes are prone to this type of instability, including CC discretizations.

Acknowledgment

Supported by the NASA Fundamental Aeronautics Program, Supersonics Project, contract NNL07AA23C (Principal Investigator: N. K. Yamaleev).

References

[1] Delanaye, M., and Liu, Y., "Quadratic Reconstruction Finite Volume Schemes on 3D Arbitrary Unstructured Polyhedral Grids," 14th AIAA CFD Conference, Norfolk, VA, AIAA Paper 1999-3259, June 1999.

[2] Mavriplis, D. J., "Unstructured Mesh Discretizations and Solvers for Computational Aerodynamics," 18th AIAA CFD Conference, Miami, FL, AIAA Paper 2007-3955, June 2007.

[3] Diskin, B., Thomas, J. L., Nielsen, E. J., Nishikawa, H., and White, J. A., "Comparison of Node-Centered and Cell-Centered Unstructured Finite-Volume Discretizations: Viscous Fluxes," *AIAA Journal*, Vol. 48, No. 7, 2010, pp. 1326–1338. doi:10.2514/1.44940; also AIAA Paper 2009-0059.

[4] Thomas, J. L., Diskin, B., and Rumsey, C. L., "Towards Verification of Unstructured-Grid Solvers," *AIAA Journal*, Vol. 46, No. 12, Dec. 2008, pp. 3070–3079. doi:10.2514/1.36655

[5] Roe, P. L., "Approximate Riemann Solvers, Parameter Vectors, and Difference Schemes," *Journal of Computational Physics*, Vol. 43, No. 2, 1981, pp. 357–372. doi:10.1016/0021-9991(81)90128-5

[6] Aftosmis, M., Gaitonde, D., and Tavares, T. S., "Behavior of Linear Reconstruction Techniques on Unstructured Meshes," *AIAA Journal*, Vol. 33, No. 11, 1995, pp. 2038–2049. doi:10.2514/3.12945

[7] Diskin, B., and Thomas, J. L., "Accuracy Analysis for Mixed-Element Finite-Volume Discretization Schemes," National Inst. of Aerospace, Rept. NIA 2007-08, Hampton, VA, Aug. 2007.

[8] Holmes, D. G., and Connell, S. D., "Solution of the 2D Navier–Stokes Equations on Unstructured Adaptive Grids," 9th AIAA CFD conference, Washington, DC, AIAA Paper 1989-1392, June 1989.

[9] Rausch, R. D., Batina, J. T., and Yang, H. T., "Spatial Adaptation Procedures on Unstructured Meshes for Accurate Unsteady Aerodynamic Flow Computation," 9th AIAA CFD Conference, Washington, DC, AIAA Paper 1989-1392, June 1989.

[10] Frink, N. T., "Recent Progress Toward a Three-Dimensional Unstructured Navier–Stokes Flow Solver," 32nd AIAA Aerospace Science Meeting and Exhibit, Reno, NV, AIAA Paper 1994-0061, Jan. 1994.

[11] Haselbacher, A. C., "On Constrained Reconstruction Operators," 44th AIAA Aerospace Science Meeting and Exhibit, Reno, NV, AIAA Paper 2006-1274, Jan. 2006.

[12] Barth, T. J., "Numerical Aspects of Computing High-Reynolds Number Flow on Unstructured Meshes," 29th AIAA Aerospace Science Meeting, Reno, NV, AIAA Paper 1991-0721, Jan. 1991.

[13] Coirier, W. J., "An Adaptively-Refined, Cartesian, Cell-Based Scheme for the Euler and Navier–Stokes Equations," NASA TM 106754, Oct. 1994.

[14] Frink, N. T., "Tetrahedral Unstructured Navier–Stokes Methods for Turbulent Flows," *AIAA Journal*, Vol. 36, No. 11, 1998, pp. 1975–1982.

doi:10.2514/2.324

[15] Diskin, B., and Thomas, J. L., "Comparison of Node-Centered and Cell-Centered Unstructured Finite-Volume Discretizations: Inviscid Fluxes," 48th AIAA Aerospace Science Meeting, Orlando, FL, AIAA Paper 2010-1079, Jan. 2010.

[16] Diskin, B., and Thomas, J. L., "Half-Space Analysis of the Defect-Correction Method for Fromm Discretization of Convection," *SIAM Journal on Scientific Computing*, Vol. 22, No. 2, 2000, pp. 633–655. doi:10.1137/S1064827599358637

[17] Smith, T. M., Barone, M. F., Bond, R. B., Lorber, A. A., and Baur, D. G., "Comparison of Reconstruction Techniques for Unstructured Mesh Vertex Centered Finite Volume Scheme," 18th AIAA CFD Conference, Miami, FL, AIAA Paper 2007-3958, June 2007.

[18] Diskin, B., and Thomas, J. L., "Accuracy of Gradient Reconstruction on Grids with High Aspect Ratio," National Inst. of Aerospace Rept. NIA 2008-12, Hampton, VA, Dec. 2008.

[19] Mavriplis, D. J., "Revisiting the Least-Square Procedure for Gradient Reconstruction on unstructured Meshes," 18th AIAA CFD conference, Orlando, FL, AIAA Paper 2003-3986, June 2003.

[20] Petrovskaya, N. V., "The Choice of Weight Coefficients for Least-Square Gradient Approximation," *Journal of Mathematical Modeling*, Vol. 16, No. 5, 2004, pp. 83–93.

[21] Mitchell, C. R., "Improved Reconstruction Schemes for the Navier–Stokes Equations on Unstructured Grids," 32nd AIAA Aerospace Science Meeting and Exhibit, Reno, NV, AIAA Paper 1994-0642, Jan. 1994.

Z. J. Wang
Associate Editor